JOURNAL OF MAGNETIC RESONANCE IMAGING 12:46–67 (2000)

Original Research

Sensitivity and Power Deposition in a High-Field Imaging Experiment

David I. Hoult, MA, D Phil*

Image signal-to-noise ratio and power dissipation are investigated theoretically up to 400 MHz. While the text is mathematical, the figures give insights into predictions. Hertz potential is introduced for probe modeling where charge separation cannot be ignored. Using a spherical geometry, the potential from current loops that would produce a homogeneous *static* B_1 field is calculated; at high frequency it is shown to create an unnecessarily inhomogeneous field. However, a totally homogeneous field is shown to be unattainable. Boundary conditions are solved for circularly polarized fields, and strategies for limited shimming of the sample B_1 field are then presented. A distinction is drawn between dielectric resonance and spatial field focusing. At high frequency, the region of maximum specific absorption is shown to move inside the sample and decrease. From the fields in both rotating frames, the signal-to-noise ratio is derived and compared with the traditional, low-frequency formulation. On average, it is mostly found to be slightly larger at high frequency. Nevertheless, the free induction decay is sometimes found to be annulled. J. Magn. Reson. Imaging 2000;12:46–67.

Index terms: imaging, high field; signal-to-noise ratio; power; SAR; dielectric resonance; field focusing

SINCE THE EARLY DAYS of human imaging, it has been known that the electrical characteristics of tissue could adversely affect the fidelity of its image. Thus, Bottomley and Andrew (1) surmised that B_1 field "penetration effects" could set an effective limit to the Larmor frequency of roughly 20 MHz, while independently but for the same reasons, Hoult and Lauterbur (2), in their paper on the signal-to-noise ratio (S/N) of the imaging experiment, suggested 10 MHz (~0.25 T for protons) as a limit. Mansfield and Morris (3) adopted the same stance. This pessimism stemmed from the fact that early images were obtained from the amplitude Fourier transform of the free induction decay (FID) in the presence of a "read" gradient. The phase of the transform had to be carefully selected to obtain the absorption mode, for the dispersion mode is not a representation of sample concentration versus distance. Thus if the phase were to vary over the sample, it would be impossible to obtain a good image. Bottomley and Andrew (1) suggested employing a power spectrum, which uses the sum of the squares of the absorption and dispersion spectra, but this suggestion was generally not well received (3), as it degrades resolution and fidelity.

An additional factor that compounded the impression of a 10-MHz barrier was the difficulty of making suitable radiofrequency (RF) coils (4). Nowadays, this "barrier" seems laughable, and with the benefit of hindsight, two developments seem to the author to have laid the foundations for breaking it. The first was the use of distributed capacitors in probe fabrication by Alderman and Grant (5), which ameliorated the coil problems. The second was the introduction by Bydder et al (6) of the Fourier transform of a symmetric echo, which contains no dispersive component. Thereafter, fields were increased to the point where we have recently seen human imaging performed at 8 T by Robitaille et al (7,8).

At such high fields, to gain insight into the manner in which B_1 fields (and hence power deposition and S/N) behave in the human body, it is essential to solve Maxwell's equations therein. There is no reason to believe, as Robitaille has posited, that some unknown physical phenomenon is at work. However, this is no easy matter, as a person is a heterogeneous mix of tissues with various conductivities and dielectric constants. At the present time, the only way to tackle a problem of this complexity is by the burgeoning discipline of electromagnetic field computational simulation (9), and while beautiful results have been obtained (10), it is all too easy for mistakes to be made in the programming and very difficult for other researchers to verify results. Thus analytical solutions to simpler models still have a considerable role to play, not only as a means of checking simulations but also in providing insights and demonstrating trends. As long ago as 1976, the author attempted to execute a full solution of Maxwell's equations for the simplest of head phantoms—a conducting sphere of high dielectric constant—and failed. The consolation prize was the realization that at the frequencies that then seemed viable (ie, <10 MHz), a pseudo-static solution was all that was needed, and thus was born the theory presented in ref. 2, which has endured as a

Institute for Biodiagnostics, National Research Council of Canada, Winnipeg, Manitoba, R3B 1Y6, Canada.

Presented at the 7th Scientific Meeting of the ISMRM, Philadelphia, 1999.

*Address reprint requests to: D.I.H., Institute for Biodiagnostics, National Research Council of Canada, 435 Ellice Avenue, Winnipeg, Manitoba, R3B 1Y6, Canada.

Received February 11, 2000; Accepted March 15, 2000.

model for S/N and power dissipation because of its simplicity and because of surprising robustness up to frequencies as high as 80 MHz.

Others were more successful in their pursuit of analytical solutions of Maxwell's equations for simple models, commencing with Bottomley and Andrew in the paper already mentioned (1), who worked with cylindrical tissue samples. They showed that one could expect a lessening of the power dependence on frequency at higher frequencies (>100 MHz), as observed by Robitaille (7,8). This work was expanded by Mansfield and Morris (2) and others while Edelstein et al (11) showed that if coil losses were negligible, the sample tended to dictate its own "intrinsic" S/N. The impetus for field analysis was increased when Glover et al (12) showed in 1985 experimental images obtained at 64 MHz containing artifacts clearly attributable to penetration effects. Obtained with a linear field probe, these artifacts appeared to violate the symmetries expected when using magnetic fields and vanished when a quadrature probe, giving a circularly polarized B_1 field, was used. As a result of this work, and the increased S/N ratio and efficient use of power expected with a circularly polarized field (13), use of the latter has ever since been *de rigueur* when imaging with volume coils at fields greater than roughly 1 T, and should also be in any theoretical calculation of S/N. The authors were able to explain their results on the basis of a cylindrical analytical model by calculating the B_1 field in the rotating frame, and Chen and Hoult (14) also explained the results with a spherical analytical model, using a low-order expansion in zonal spherical Bessel harmonics inside the sample and a homogeneous field outside. The z axis became the direction of their linear B_1 field, and a circularly polarized field was described by a rotation of the lowest order fields by 90°. Further experimental evidence was provided in 1988 by Bomsdorf et al (15), who showed substantial field focusing effects in 4-T images of water. However, they found no sign of such effects in images of the human head. They can, however, be seen in Robitaille's work.

Theoretical advances were made by Carlson (16), who was mainly interested in power deposition and noise correlation, and by Keltner and Carlson and their colleagues (17). While the latter paper introduces a formalism that may be used with quadrature coils, it was then restricted to an analysis with a surface coil in zonal harmonics, ie, there was symmetry about the z axis. Furthermore, there was no attempt to describe fields in the rotating frame, which is essential if a full understanding of image artifacts and S/N is to be obtained. However, the paper is notable in that for the first time, to the best of the author's knowledge, it was not assumed that the driving field from the probe was quasistatic, ie, expressible as an expansion in spherical harmonics. The latter is acceptable when the diameter of the sample is much less than a wavelength in free space, but at 340 MHz (8 T), we are no longer in that situation, and this fact must be recognized from the outset in calculations. We shall see that even *in vacuo*, higher order terms are always present with a probe that ostensibly delivers a homogeneous field.

In a separate development using a plane wave approach, Ocali and Atalar (18) have shown how to calculate at any frequency the fields that give in a model the best S/N ratio at some position of interest. Although this is innovative and novel work, their method does not allow one to calculate analytically the power deposition and S/N when using a known quadrature probe. It should also be pointed out that all studies to date make assumptions as to the nature of the driving field and the manner in which it is derived. First, some workers have only specified the driving B_1 field, rather than the current that creates it. Thus a multipole field expansion ignores the fact that various orders are coupled, and there is then the danger, as mentioned above, of omitting higher order terms. Second, the problem that made early researchers feel that probes could not be fabricated at high frequency is typically ignored—the separation of charge that occurs when the length of conductors is not very much less than a wavelength.

Ultimately, the present discussion will also work around this problem, which requires that scalar as well as vector potential be used in a mathematical description. However, it will introduce for future use a formalism needed to cope with this difficulty—the Hertz potential. Thus the purpose of the present work is to fill a gap in the literature and give insight into the manner in which power deposition and S/N vary spatially and with frequency in the quadrature imaging experiment with a volume coil. To this end, the model we shall use is that of a conducting sphere of high dielectric constant surrounded by a spherical probe. It is stressed that this model is poor both in its absence of sample heterogeneity and its use of currents on the surface of a sphere rather than on that of a cylinder. However, it *is* analytically soluble! Of necessity, the mathematics in this paper is compressed, but not so much that only a handful of experts can follow it and reproduce the conclusions. Furthermore, once the mathematics is fully in place, it should be possible to stay with its philosophy while transferring the probe to the surface of a cylinder (19). For those readers who do not wish to trudge through the equations, the article has a number of helpful figures (with fuller legends than usual) that should convey the progression of the analysis.

Finally, a word of explanation as to the structure of some of the figures. In covering the frequency range up to 400 MHz, there is a large dynamic range (up to 10^5) in some of the variables to be displayed; showing the full range obscures points of interest—they become negligible in the grand scheme. Thus in Figs. 10b, 11, and 12, which display power and S/N, these quantities have been shown *in comparison* with the values predicted by the low-frequency "traditional" formulae (2). The latter have the huge advantage of being easily calculable—at a stretch by hand. Thus the figures essentially show how much the traditional approach is in error and by what factor. In the case of power (Fig. 10b), the ratio is shown in dB, as power is set on many consoles in these units and they should therefore be familiar. However, in Fig. 12, notwithstanding the use of a ratio, a meaningful display of signal strength could only be obtained if a logarithmic scale was used. Thus a dB scale was again employed, and it is hoped that this

will not cause confusion for readers who are not that familiar with these engineering units.

THEORY

Basic Electromagnetism

We shall consider at frequencies up to 400 MHz a spherical "head," or, more specifically, a conducting sphere whose dielectric constant ϵ is 80 and whose conductivity σ ranges from 0 to 1 Sm^{-1}—roughly the range of values found in human tissue. We have not allowed the dielectric constant to vary. *Under the conditions prescribed in this paper*, for most relative results such as images which do not have a fixed brightness scale, such variation can be taken into account simply by changing the frequency and the conductivity—see the legend to Fig. 4 and Eq. [30] et seq. The path we shall take is as follows:

1. Introduce for future use the Hertz potential as a means of dealing with both scalar and vector potential in a single variable.
2. Indicate the solutions of the full Maxwell equations for the sample and in free space.
3. Find the Hertz potential of an elementary current loop on the surface of a sphere surrounding our sample.
4. Use a distribution of such loops to create in the *xy* plane, not along the *z* axis, an alternating, linearly polarized B_1 driving field that at low frequencies would be totally homogeneous.
5. Solve the boundary value problem to obtain the electric and magnetic fields inside the sample.
6. Find the equivalent fields for a circularly polarized B_1 driving field.
7. Calculate the power deposited and its dependencies.
8. Find the S/N with the aid of the Principle of Reciprocity.

We shall also take a diversion to show how to obtain the current distribution needed to generate homogeneous B_1 fields in the sample rotating frame, in the limited circumstances in which it is possible to do so.

Maxwell's equations in the Lorentz gauge in a conducting medium yield a damped wave equation for induction field **B**, electric field **E**, vector potential **A**, and scalar potential Φ, of the form (20):

$$\nabla^2\Xi = \mu\mu_0\sigma\frac{\partial\Xi}{\partial t} + \mu\mu_0\epsilon\epsilon_0\frac{\partial^2\Xi}{\partial t^2}, \qquad (1)$$

Here, Ξ is a general variable, μ_0 and ϵ_0 are respectively the permeability and permittivity of free space, μ and ϵ are respectively the relative permeability and permittivity of the medium, σ is the medium's conductivity, and *t* is time. S.I. units are assumed. Eq. [1] also applies to the Cartesian components of the fields and potentials. However, if there is a particular region in which there is a current source of density **J**, but outside that region the conductivity σ is zero, then $\mathbf{J} = \sigma\mathbf{E}$, and the equation for the vector potential becomes:

$$\nabla^2\mathbf{A} - \mu\mu_0\epsilon\epsilon_0\frac{\partial^2\mathbf{A}}{\partial t^2} = -\mu\mu_0\mathbf{J}. \qquad (2)$$

Thus the current **J** "drives" the differential equation.

These equations may be found in any good electromagnetics text (20–22), but we now turn to a less well-trodden path and following Hertz (22,23), define a new vector potential $\mathbf{\Pi}$ where:

$$\mathbf{A} = \mu\mu_0\sigma\mathbf{\Pi} + \mu\mu_0\epsilon\epsilon_0\frac{\partial\mathbf{\Pi}}{\partial t}, \qquad (3)$$

$$\Phi = -\nabla\cdot\mathbf{\Pi}. \qquad (4)$$

By direct substitution, it may be shown that this Hertz potential can only satisfy Eq. [1] in **A** and Φ if:

$$\nabla^2\mathbf{\Pi} = \mu\mu_0\sigma\frac{\partial\mathbf{\Pi}}{\partial t} + \mu\mu_0\epsilon\epsilon_0\frac{\partial^2\mathbf{\Pi}}{\partial t^2}. \qquad (5)$$

Thus $\mathbf{\Pi}$ and its Cartesian components also obey Eq. [1]. By using this potential, we incorporate both scalar and vector potential in one variable and in so doing, anticipate future calculations and numerical simulations that accommodate charge separation in the probe and sample. For example, a probe comprising individually driven dipole antennae in an array might conceivably be employed for some reason! The use of a single variable would then effect a major simplification, as it would for probes comprising clusters of loops of significant ($>\lambda/20$) length.

Continuing, let it be tacitly understood that all variables fluctuate as $\exp(i\omega_0 t)$ where *i* is the square root of minus one and ω_0 is the frequency of interest—usually the Larmor frequency. A positive exponent is used for compatibility with the transition later to a positively rotating frame. Then Eq. [1] reduces to the Helmholtz equation:

$$\nabla^2\Xi + k^2\Xi = 0; \quad k^2 = \omega_0^2\mu\mu_0\epsilon\epsilon_0 - i\omega_0\mu\mu_0\sigma, \qquad (6)$$

where *k* is the complex wavenumber, and it is worth noting that for a saline sphere with $\sigma = 0.5$ Sm^{-1}, the real part of the expression for k^2 predominates above 132 MHz. We are now in a position to define the terms "low" and "high" frequency. For the rest of the article, "low frequency" implies that $|ka| << 1$ and "high frequency" implies that $|ka| \sim 1$ or greater, where *a* is the radius of the sample. Continuing, from Eq. [3] it follows that:

$$\mathbf{A} = (\mu\mu_0\sigma + i\mu\mu_0\epsilon\epsilon_0\omega_0)\mathbf{\Pi} = \frac{ik^2\mathbf{\Pi}}{\omega_0}, \qquad (7)$$

and hence, as $\mathbf{B} = \text{curl}\ \mathbf{A}$:

$$\mathbf{B} = \frac{ik^2}{\omega_0}\nabla\wedge\mathbf{\Pi}. \qquad (8)$$

We further note that from Eqs. [4] and [7], as (20,21)

$$\mathbf{E} = -\frac{\partial \mathbf{A}}{\partial t} - \nabla\Phi:$$

$$\mathbf{E} = k^2\mathbf{\Pi} + \nabla(\nabla \cdot \mathbf{\Pi}) = \nabla \wedge \nabla \wedge \mathbf{\Pi}. \tag{9}$$

It follows that by invoking the Hertz vector, we have simple access to both the magnetic and electric fields even if there is charge separation on the conductor or in the sample. Note that if $\nabla \cdot \mathbf{\Pi} = 0$, and the charge separation can be neglected, then:

$$\mathbf{E} = k^2\mathbf{\Pi}. \tag{10}$$

Hertz Basis Vectors

Eigenfunction solutions of the Helmholtz equation [6], in the spherical polar coordinates (r, θ, ϕ) appropriate to our choice of sample, are well known (9,21,24). They are spherical Bessel harmonics of the general form:

$$\Xi = f_n(kr)P_{n,m}(\cos\ \theta)^{\cos m\phi}_{\sin m\phi}, \tag{11}$$

where $P_{n,m}(\cos\theta)$ is Ferrer's associated Legendre polynomial of order n and degree m, and $f_n(kr)$ stands for one of the three kinds of spherical Bessel functions (22) of order n:

$$j_n(kr) = \left[\frac{\pi}{2kr}\right]^{1/2} J_{n+1/2}(kr)$$

$$y_n(kr) = \left[\frac{\pi}{2kr}\right]^{1/2} Y_{n+1/2}(kr) \tag{12}$$

$$\begin{cases} h_n^{(1)}(kr) = j_n(kr) + iy_n(kr) \\ h_n^{(2)}(kr) = j_n(kr) - iy_n(kr). \end{cases}$$

J and Y are the ordinary Bessel functions of the first and second kinds, respectively, and h is sometimes referred to as the spherical Hankel function. We shall be particularly interested in the solutions:

$$\begin{aligned} S_{n,m} &= h_n^{(2)}(kr)P_{n,m}(\cos\ \theta)\cos\ m\phi; \\ T_{n,m} &= h_n^{(2)}(kr)P_{n,m}(\cos\ \theta)\sin\ m\phi; \\ U_{n,m} &= j_n(kr)P_{n,m}(\cos\ \theta)\cos\ m\phi; \\ V_{n,m} &= j_n(kr)P_{n,m}(\cos\ \theta)\sin\ m\phi. \end{aligned} \tag{13}$$

S and T are applicable away from the origin, for there they are infinite, while U and V are applicable about the origin where they are finite. Note that for $j_n(kr)$ when $kr << 1$ and for $h_n^{(2)}(kr)$ when $kr >> 1$,

$$j_0(kr) \approx 1 - \frac{k^2r^2}{6}; \quad j_1(kr) \approx \frac{kr}{3}; \quad j_2(kr) \approx \frac{k^2r^2}{15};$$

$$h_1^{(2)}(kr) \approx \frac{i}{k^2r^2}; \quad h_2^{(2)}(kr) \approx \frac{3i}{k^3r^3}. \tag{14}$$

Hence as $kr \to 0$ (in other words, at low frequency), the harmonic $U_{0,0} \to 1$, and thus this solution for the magnetic field B_x represents a homogeneous B_1 field. (Remember that solutions are valid for Cartesian field components even though the coordinate system used is polar.) However, as kr approaches unity and the wavelength in the sample becomes comparable with the latter's dimensions, $U_{0,0}$ begins to have spatial dependence.

Having solved Maxwell's equations as an expansion of terms such as $U_{n,m}$ having various orders and degrees, Fig. 1 shows, in vacuo, in pure water (dielectric constant 80) and in water with a conductivity of unity, the behavior of the lowest order B_1 field, $U_{0,0}$, plotted as a function of radius and frequency. There is not too much inhomogeneity in the field in vacuo, at least up to 400 MHz, but the plot in water at high frequency appears to exhibit "field focusing" wherein the field is much larger at the origin (15); sample conductivity appears to dampen the effect. (Note that this effect is sometimes incorrectly termed "dielectric resonance." We shall see later an example of the latter phenomenon.) However, we must not assume that the field $U_{0,0}$ is an adequate descriptor of field focusing, for it is quite possible that at high frequency, additional, higher order terms are manifest in the B_1 field inside our sphere, even if it is driven with an ostensibly homogeneous field. Indeed, the experiments of Glover et al (12) mentioned earlier emphasize this point. They observed azimuthal asymmetry; $U_{0,0}$ is, in contrast, symmetric and somehow, symmetry is broken.

It follows that considerable care must be taken with any derivation and so we now first calculate the fields created in free space by an appropriate distribution of alternating current on the surface of a larger sphere surrounding our saline sphere—a convenient mathematical construct for simulating a high-frequency probe. We shall then find the fields inside the smaller sample. Others may wish to use a distribution on a cylinder or some other surface (19). However, a change of surface will not affect the general conclusions we shall come to, as these are determined by the nature of Maxwell's equations in space and in the sample.

Consider a current element Ids at point Q on the surface of a sphere, of radius b greater than that a of our sample, at spherical coordinates (b,α,ψ), as shown in Fig. 2. In the temporary absence of the sample, at point $P(r,\theta,\phi)$, a distance R away, it may be shown from Eqs. [2] and [3] that the Hertz potential $\mathbf{\Pi}$ is given by (21,24):

$$d\mathbf{\Pi} = -i\,\frac{\omega_0\mu_0 I}{4\pi k_e^2}\,\frac{e^{i(\omega_0 t - k_e R)}}{R}\,d\mathbf{s}, \tag{15}$$

where k_e is the wavenumber k in free space and $k_e = \omega_0(\epsilon_0\mu_0)^{1/2} = 2\pi/\lambda$ where λ is the wavelength there. Interestingly, the Hertz potential of Eq. [15] cannot be split into "near" and "far" components; it contains only a propagator that, if we were describing a field, would be termed "far field." The Green's function $\exp(-ik_eR)/R$

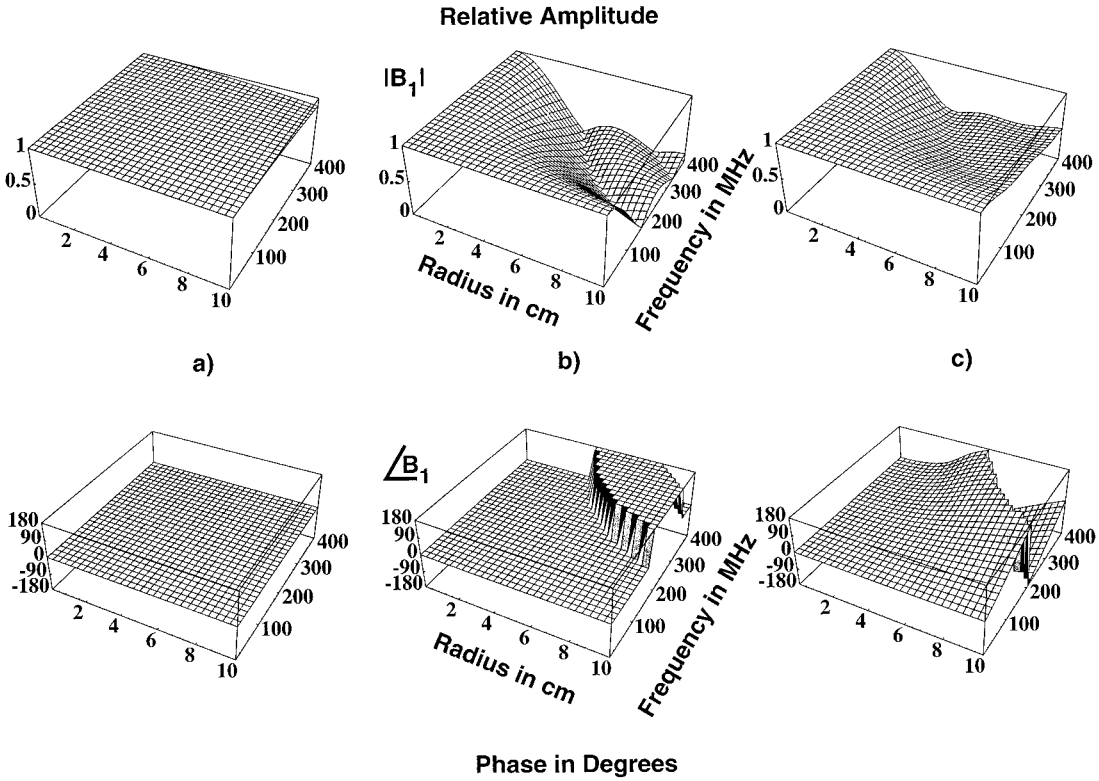

Figure 1. Variation of the spherical Bessel harmonic $U_{0,0}$ with radius and frequency. **a:** In vacuo. **b:** In pure water with a dielectric constant of 80. **c:** In saline with a conductivity of 1 Sm^{-1}. At frequencies where the wavelength of radio waves *in the sample* is comparable to the sample size, it no longer suffices to describe B_1 magnetic fields by simple expansions such as a Taylor series, rather, for a spherical sample one must use an expansion in spherical Bessel harmonics—a combination of Bessel functions, associated Legendre polynomials, and trigonometric functions. With any expansion, one assumes that as the arguments tend to zero, it is the lowest order terms that prevail and so the figure shows how the lowest order term varies with radius and frequency. (In fact, it is shown later that it is impossible for the lowest order term to exist by itself, but the next term in the expansion does not make a large difference to the plots.) In a, it is clear that in vacuo there is very little variation in field strength with radius, even at 400 MHz, up to a radius of 10 cm. This is also so in water at low frequencies, as seen in b. At high frequencies, however, there is great inhomogeneity in the field—so-called field-focusing (not to be confused with dielectric resonance—see Fig. 6) that makes the field at the origin much stronger than further out in the sample. The focusing effect is dampened in c by the conductivity of the saline, and the field at 400 MHz and 10 cm has risen appreciably compared with that in b. With higher and higher conductivities (not shown), the field at the sample edge rises further and further until (with, eg, a metal) it is much greater at the sample surface than at the center, the so-called skin effect.

may be expanded in terms of spherical Bessel harmonics (21,24). When $r < b$, it is:

$$\exp(-ik_e R)/R$$

$$= -ik_e \sum_{n=0}^{\infty} \sum_{m=0}^{n} \epsilon_m (2n+1) \frac{(n-m)!}{(n+m)!} j_n(k_e r)$$

$$\times h_n^{(2)}(k_e b) P_{n,m}(\cos\alpha) P_{n,m}(\cos\theta) \cos[m(\phi - \psi)], \quad (16)$$

where the Neumann function ϵ_m is 1 if $m = 0$ and otherwise 2. In preparation for "constructing" a probe made of a large array of individually driven current loops, we now use Eqs. [15] and [16] to calculate the Hertz potential of a small loop of current lying at some arbitrary position on the surface of the sphere, as shown in Fig. 2. (A different method of finding the fields from such a ring placed at a *pole* of the sphere is given by Jin (9) and Keltner et al (17). However, their method of calculation in zonal ($m = 0$) harmonics cannot easily accommodate circularly polarized fields and was used only with a surface coil.) It is at this point that the author is perhaps "cheating," for a small ($<<\lambda$) loop has negligible charge separation and therefore the scalar potential will also be negligible. Thus the fields from an array of such loops will not be exactly the same as those from a bulk probe. However, such a loop *is* a physically realizable current distribution, and it may well be that an array thereof constitutes a good method of constructing a body coil at 8 T—precisely because the conservative electric fields of each loop are small. The theory and practice ride hand in hand. At any rate, its use should give a valid insight into field behavior. A summary of the calculation is given in the Appendix, where it is shown that for an outwardly pointing current dipole $\mathfrak{m}$ at point $Q(b,\alpha,\psi)$, the Cartesian components [Π_x, Π_y, Π_z] of vector potential $\mathbf{\Pi}$ at point P are:

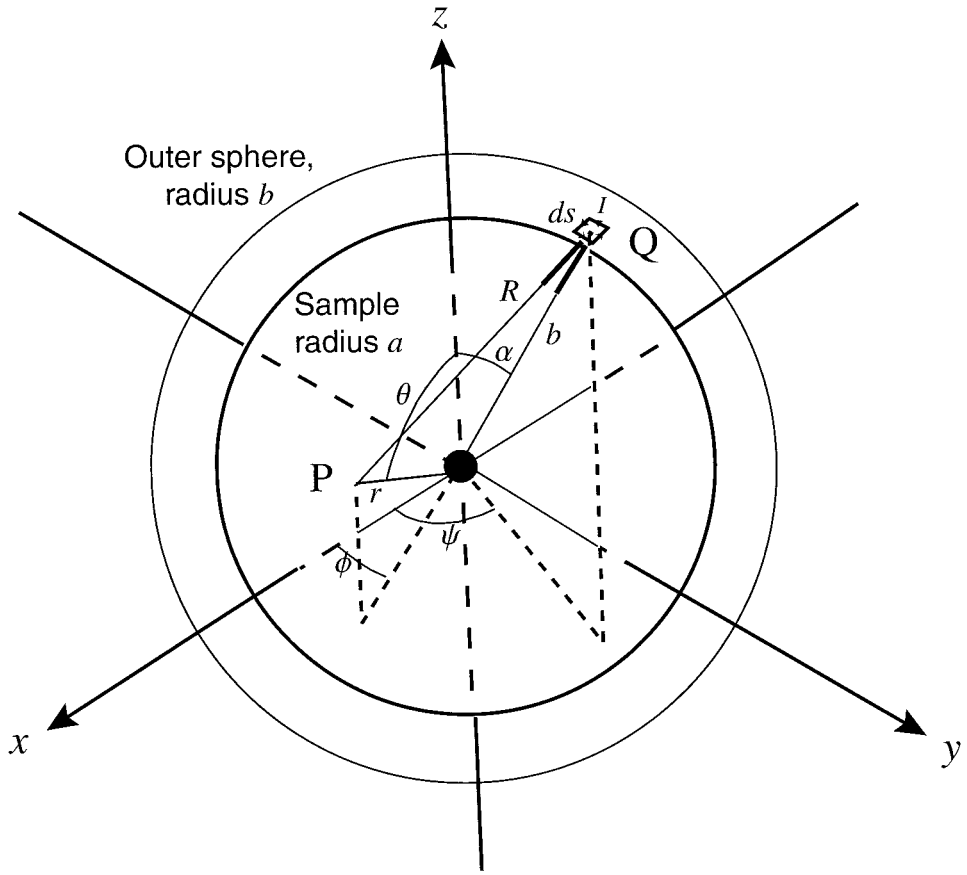

Figure 2. The coordinate system. The B_1 field in the sample is considered, for mathematical purposes, to be generated by many tiny current loops on the surface of an outer sphere encompassing the sample. Later, we shall allow the loop currents to vary in amplitude and phase with position on the sphere so as to generate desired field distributions. However, for the time being, a single loop is shown at point *Q* at spherical polar coordinates (b, α, ψ), and the field at another point P(r, θ, ϕ), a distance R away, can then be calculated. To aid in the calculation, the loop is considered to be a square of side ds, carrying current I, and the sides of the square are parallel to lines of latitude and longitude. The loop's magnetic moment is $\mathfrak{m} = \mathrm{I}ds^2$.

$$\mathbf{\Pi} = \mathfrak{m} \sum_{n=0}^{\infty} \sum_{m=0}^{n} \chi_{n,m}$$

$$\begin{bmatrix} (n+m)(n-m+1)\varsigma_m U_{n,m} T_{n,m-1} \\ \quad -(n+m)(n-m+1) V_{n,m} S_{n,m-1} \\ \quad +\eta_m U_{n,m} T_{n,m+1} - V_{n,m} S_{n,m+1}, \\ (n+m)(n-m+1)\varsigma_m U_{n,m} S_{n,m-1} \\ \quad +(n+m)(n-m+1) V_{n,m} T_{n,m-1} \\ \quad -\eta_m U_{n,m} S_{n,m+1} - V_{n,m} T_{n,m+1}, \\ -2mU_{n,m} T_{n,m} + 2mV_{n,m} S_{n,m} \end{bmatrix} \qquad (17)$$

where the brackets contain the Cartesian 3-vector, ς_m is zero if $m = 0$ and one otherwise, η_m is two if $m = 0$ and one otherwise, and constants $\chi_{n,m}$ are given by:

$$\chi_{n,m} = \frac{-\omega_0 \mu_0}{8\pi b k_e} \epsilon_m (2n+1) \frac{(n-m)!}{(n+m)!}. \qquad (18)$$

As $r < b$, U and V are functions of [r,θ,ϕ] while S and T are functions of [b,α,ψ].

With this formula, we have a "building block" for the construction of specific B_1 magnetic fields. To proceed, we must be able to take the potential's curl (see Eqs. [8] and [9]), and this implies that as we have obtained Cartesian components of $\mathbf{\Pi}$, we must be able to differentiate the spherical Bessel harmonics, expressed in polar coordinates, with respect to Cartesian coordinates x, y, and z. The necessary formulae, as given in Table 1, may be found without too much difficulty because we know that Cartesian derivatives must also be sums of spherical Bessel harmonics. The derivation is indicated in the Appendix. At first sight, this use of mixed coordinates may appear strange, but in the author's opinion, it is this approach that allows one to enter the rotating frame with little difficulty without the intrusion of projection terms such as $\sin\theta$ and $\cos\phi$ that destroy the harmonic representation. Applying the formulae of Table 1 to find the divergence of $\mathbf{\Pi}$, it may be confirmed by the reader that this quantity is, not surprisingly, zero, thanks to the use of the infinitesimal current loop, and thus the calculation could employ from now on $\mathbf{A}$ rather than $\mathbf{\Pi}$. However, the presence of charge separation would merely change the coefficients in Eq. [17] rather than necessitating the introduction of an extra variable, and so it is hoped that the usefulness of $\mathbf{\Pi}$ has been demonstrated. For consistency we remain with $\mathbf{\Pi}$ and from Eq. [8] the $\mathbf{B}$ field is

Table 1
Cartesian Differentiation of Spherical Bessel Harmonics $U_{n,m}$ and $V_{n,m}$

$$\frac{dU_{n,m}}{dx} = \frac{k}{2(2n+1)}\{(n+m)(n+m-1)\varsigma_m U_{n-1,m-1} - \varsigma_n\eta_m U_{n-1,m+1} + (n-m+1)(n-m+2)\varsigma_m U_{n+1,m-1} - \eta_m U_{n+1,m+1}\}$$

$$\frac{dU_{n,m}}{dy} = \frac{-k}{2(2n+1)}\{(n+m)(n+m-1)\varsigma_m V_{n-1,m-1} + \varsigma_n\eta_m V_{n-1,m+1} + (n-m+1)(n-m+2)\varsigma_m V_{n+1,m-1} + \eta_m V_{n+1,m+1}\}$$

$$\frac{dU_{n,m}}{dz} = \frac{k}{(2n+1)}\{(n+m)U_{n-1,m} - (n-m+1)U_{n+1,m}\}$$

$$\frac{dV_{n,m}}{dx} = \frac{k\varsigma_m}{2(2n+1)}\{(n+m)(n+m-1)V_{n-1,m-1} - \varsigma_n\eta_m V_{n-1,m+1} + (n-m+1)(n-m+2)V_{n+1,m-1} - \eta_m V_{n+1,m+1}\}$$

$$\frac{dV_{n,m}}{dy} = \frac{k\varsigma_m}{2(2n+1)}\{(n+m)(n+m-1)U_{n-1,m-1} + \varsigma_n\eta_m U_{n-1,m+1} + (n-m+1)(n-m+2)U_{n+1,m-1} + \eta_m U_{n+1,m+1}\}$$

$$\frac{dV_{n,m}}{dz} = \frac{k\varsigma_m}{(2n+1)}\{(n+m)V_{n-1,m} - (n-m+1)V_{n+1,m}\}$$

If $n < m$, $U_{n,m} = V_{n,m} = 0$. ς_q is 0 when integer q is 0; otherwise it is 1. η_q is 2 when integer q is 0; otherwise it is 1.

found, while from Eq. [10] the **E** field may be seen to be simply $k^2\mathbf{\Pi}$.

Let us now use Eq. [17] to construct a B_1 field that is homogenous at low frequency. For example, a common textbook exercise is to show that for direct currents, such a field may be produced in the x direction by coaxial rings of current equally spaced down the x axis and parallel to the yz plane that are on the surface of a sphere (20). To generate such a current distribution, we use a surface distribution of magnetic moments given by:

$$d\mathbf{m} = \Omega_1 P_{1,1}(\cos\alpha)\cos\psi d\mathbf{\Lambda} \qquad (19)$$

where Ω_1 is a constant and $d\mathbf{\Lambda}$ is an elementary vector surface area. Applying this expression for the elementary magnetic moment $d\mathbf{m}$ to Eq. [17], by the orthogonality of surface harmonics, the integral over the surface is only non-zero for Π_x and Π_y when $n = 1$, $m = 0$, and for $\mathbf{\Pi}_z$ when $n = m = 1$. Hence, the Hertz vector potential $\mathbf{\Pi}_{px}$ for a probe B_1 field that is homogeneous at low frequency and in the x direction, is given by:

$$\mathbf{\Pi}_{px} = \left(\Omega_1 \frac{\omega_0\mu_0 b}{k_e} h_1^{(2)}(k_e b)\right)[0,\ U_{1,0},\ -V_{1,1}] \equiv C_1\mathbf{\Pi}_{1x}^{(i)} \qquad (20)$$

and it should be noted that the "Hertz basis vector" of order one $\mathbf{\Pi}_{1x}^{(i)} = [0,\ U_{1,0},\ -V_{1,1}]$ also has a divergence of zero. The first-order distribution on the surface of the probe sphere has resulted in a first-order Hertz vector, a pleasing and useful correspondence that we shall see also applies to higher orders.

Notation

The reader will doubtless have noticed that the notation we are using is becoming involved, and while a major effort has been made to keep it consistent and meaningful, some clarification is required. Thus subscript "p" is fairly obvious, standing for "probe" while numerical subscripts are indicative of order n and degree m. Subscript "e" denotes that the quantity, for example k_e, is defined exterior to the sample, while subscript "i" (not yet used) will denote that a quantity is defined inside the sample. On the other hand, superscript "(e)" will denote an exterior function valid only outside the sphere of radius a or b, as appropriate, while superscript "(i)" will denote an interior function, valid only inside the sphere of radius a or b, as appropriate. Superscript "(o)" will denote that the function or quantity is defined at the origin; subscript *extensions* x or y (for example, $\mathbf{\Pi}_{1x}$) denote the primary direction of a **B** field associated with a potential. Hopefully, the only region where confusion could possibly arise is in the space between the two spheres.

From Eq. [10], we immediately know the **E** field in free space—it is simply k_e^2 times Eq. [20]. To obtain the B_1 field in the laboratory frame, albeit for the moment still in free space, we take $(ik_e^2/\omega_0)\nabla\wedge\mathbf{\Pi}_{px}$, see Eq. [8]. Even in free space, we obtain an inhomogeneous field that has higher order and degree components in all directions:

$$\mathbf{B}_{px} = C_1\left(\frac{ik_e^2}{\omega_0}\right)\nabla\wedge\mathbf{\Pi}_{1x}^{(i)}$$

$$= C_1\frac{-ik_e^3}{6\omega_0}[4U_{0,0} - 2U_{2,0} + U_{2,2},\ -V_{2,2},\ 2U_{2,1}]. \qquad (21)$$

It cannot be stressed too strongly that it is incorrect to assume that a field that has a simple static spatial variation described by, for example, a single spherical harmonic has an equally simple description at high frequency. This is clearly not so, and we shall examine the possibility of creating a sole spherical Bessel harmonic later. Meanwhile, in the low frequency limit as $k_e \to 0$,only the term $U_{0,0}$ contributes to the field, and the latter becomes homogeneous. From Eq. [14], if $\Omega_1 = 1$:

$$\lim_{k_e\to 0}[\mathbf{B}_{px}] = \frac{2\mu_0}{3b}\hat{\mathbf{x}}, \qquad (22)$$

where $\hat{\mathbf{x}}$ is the unit vector in the x direction. This result is easily shown to be the answer that one would expect from a simple application of the Biot-Savart formula (20).

BOUNDARY CONDITIONS

So far, we have generated, by virtue of currents or magnetic moments on the surface of our outer sphere, a B_1 field in vacuo in the laboratory frame that at low frequency is homogeneous and in the x direction. We have also shown, however, that not only does the function that describes that homogeneous field generate an inhomogeneous field at high frequency, but that there is at this point also a variety of extra, higher order terms that take on significance, all resulting from a first-order Hertz basis vector. They make the field even more inhomogeneous and the higher the frequency, the more these terms become significant.

We now replace our sample, which we had temporarily removed, consider the boundary conditions at the surface of the conducting sphere of high dielectric constant, and calculate the fields within. Those fields cause conduction and displacement currents to flow, which in turn produce additional fields inside and outside. Outside the sample, the appropriate basis vectors $\mathbf{\Pi}_n^{(e)}$ for fields produced by currents within may be created by substituting function S for U and function T for V in $\mathbf{\Pi}_n^{(i)}$. This is a consequence of the reciprocal nature of the Green's function and is discussed in detail in the text by Morse and Feshbach (21). The applicable boundary conditions are the Dirichlet conditions that the surface-tangential component of $\mathbf{E}$ and all components of $\mathbf{B}$ (as $\mu = 1$) must be continuous across the boundary, and the Neumann condition that dB_x/dx must be continuous at $x = a$. However, it is easily shown that $\mathbf{\Pi}_{nx}$ have no surface-normal components, as we would expect given that there is symmetry about the x axis with zero divergence. Thus, equating respectively inner and outer tangential electric fields at the surface of the sphere, from Eq. [10]:

$$\sum_{n=1,3,\ldots}^{\infty} k_i^2 F_n \mathbf{\Pi}_{nx}^{(i)} = C_1 k_e^2 \mathbf{\Pi}_{1x}^{(i)} + \sum_{n=1,3,\ldots}^{\infty} k_e^2 G_n \mathbf{\Pi}_{nx}^{(e)}, \qquad (23)$$

where the wavenumber $k_i^2 = \omega_0^2 \mu\mu_0 \epsilon\epsilon_0 - i\omega_0 \mu\mu_0 \sigma$, the F_n on the left-hand side are constants pertaining to inside the sphere and the G_n on the right-hand side are constants pertaining to the exterior of the sphere. The exterior first-order "driving" field, created by the current loops on the outer sphere of radius b, has amplitude C_1. Note that there is no linkage between electric fields of different orders in this equation, and so we may separate the various orders.

Turning to the $\mathbf{B}$ fields, we may equate the various Cartesian components at the surface. Furthermore, by the orthogonality of surface harmonics, we may equate not just Cartesian *components*, but within those components, the various orders and degrees. Thus, with reference to Eq. [20] and Table 1, if we choose to equate zeroth order internal and external components at the surface, these must arise only from first-order internal and external Hertz vectors, and we have:

$$k_i^3 F_1 j_0(k_i a) = k_e^3 \{C_1 j_0(k_e a) + G_1 h_0^{(2)}(k_e a)\} \qquad (24)$$

From Eqs. [23] and [24] we can obtain the values of constants F_1 and G_1 in terms of the strength C_1 of the probe field, and in particular, inside the sample:

$$F_1 = \frac{k_e^3 (h_0^{(2)}(k_e a) j_1(k_e a) - h_1^{(2)}(k_e a) j_0(k_e a))}{k_i^2 (k_e h_0^{(2)}(k_e a) j_1(k_i a) - k_i h_1^{(2)}(k_e a) j_0(k_i a))} C_1$$

$$\equiv \beta_1 C_1. \qquad (25)$$

Moving now to the second-order magnetic fields, these are associated with both $\mathbf{\Pi}_1$ and $\mathbf{\Pi}_3$. Equating at the surface the various harmonics of second order, we therefore obtain the expression:

$$k_i^3 \{F_1 j_2(k_i a) + O_3^{(i)}(k_i a)\}$$

$$= k_e^3 \{C_1 j_2(k_e a) + G_1 h_2^{(2)}(k_e a) + O_3^{(e)}(k_e a)\}, \qquad (26)$$

where the $O_3(k_e a)$ terms are the fields due to $\mathbf{\Pi}_3$. Now we know that (25):

$$f_{n-1}(kr) + f_{n+1}(kr) = (2n + 1) \frac{f_n(kr)}{kr} \qquad (27)$$

Adding Eqs. [24] and [26] and applying Identity [27], we obtain:

$$k_i^3 \left\{ \frac{3F_1}{k_i a} j_1(k_i a) + O_3^{(i)}(k_i a) \right\}$$

$$= k_e^3 \left\{ \frac{3C_1}{k_e a} j_1(k_e a) + \frac{3G_1}{k_e a} h_1^{(2)}(k_e a) + O_3^{(e)}(k_e a) \right\}. \qquad (28)$$

Comparison with the first order of Eq. [23] immediately shows that we have linear dependency among the various boundary equations, leaving, from Eq. [28]:

$$k_i^3 O_3^{(i)}(k_i a) = k_e^3 O_3^{(e)}(k_e a). \qquad (29)$$

Turning to Neumann boundary conditions, we must equate the derivative of B_x with respect to x at $x = a$. However, it may be shown that this condition also reveals no connection between the first- and third-order Hertz basis vectors and is merely a repeat of an equation given by the Dirichlet conditions. We conclude that a Hertz basis vector of order one fully describes the magnetic and electric fields produced inside our sphere by application of a Hertz basis vector of order one outside the sphere created in turn by RF magnetic moments (current loops) of distribution order $n = 1$ and degree $m = 1$ on the surrounding probe sphere. In general, it may be shown that the Hertz vector of any order is homologous across the boundary—there is no coupling of orders.

Linear and Circular Polarizations

From Eqs. [21] and [25], we may now determine, for our probe, the strength of the B_1 field inside the sample in the positively rotating frame. As we have employed a time variation as $\exp(i\omega_0 t)$, it is:

$$\tilde{B}_{px}^{(+)} = \frac{B_x + iB_y}{2} = \beta_1\left(\Omega_1 \frac{-i\mu_0 b k_i^3}{3k_e} h_1^{(2)}(k_e b)\right) \times \left(U_{0,0} - \frac{U_{2,0}}{2} + \frac{U_{2,2} - iV_{2,2}}{4}\right). \quad (30)$$

Note that even though we have two different orders and two different degrees of fields here, they all have a common multiplier determined by the boundary conditions—they are linked. A change of frequency or size of sample has no effect on the *relative* sizes of the different harmonics. This subtle but important point is totally missed if the starting point of the calculation is an arbitrary set of driving fields rather than the currents in the probe. The origin of the inhomogeneities observed by Glover et al (12) is apparent in the second degree ($m = 2$) terms, as shown in Fig. 3a for our sample at 64 MHz—the frequency Glover used. At low frequency, letting $k_e \to 0$ and $k_i^2 \to -i\omega_0\mu_0\sigma$, while $|k_i b| << 1$, and setting $\theta = 90°$ so that we are in a transverse plane, we obtain, if $\Omega_1 = 1$:

$$\tilde{B}_{1\,\text{linear}}^{(+)} \to \frac{\mu_0}{3b}\left(1 - \frac{\omega_0\sigma\mu_0 r^2 \sin 2\phi}{20}\right), \quad (31)$$

which is the same result obtained by Chen and Hoult (14) after correcting the numerical error in their expansions of the spherical Bessel functions. (The factors of 1/4 in their Eqs. [4.66] through [4.68] should be 1/10.)

If we add a second B_1 field along the laboratory y axis and with quadrature phase lag relative to the field along the x axis, it is obvious by symmetry that whereas the original Hertz basis vector (Eq. [20]) was:

$$\underset{\text{cosine}}{\Pi_{1x}^{(i)}} = [0,\ U_{1,0,} - V_{1,1}]$$

the additional Hertz basis vector is:

$$\underset{\text{sine}}{\Pi_{1y}^{(i)}} = [iU_{1,0},\ 0,\ -iU_{1,1}] \quad (32)$$

Thus the total Hertz basis vector for a quadrature probe generating, at low frequency, a homogeneous, circularly polarized field is:

$$\Pi_1^{(i)} = i[U_{1,0},\ -iU_{1,0},\ -(U_{1,1} - iV_{1,1})] \quad (33)$$

and the reader is urged to note the ease with which we have produced the required vector, once we have the vector for a linearly polarized magnetic field. When we use Table 1 and Eq. [8] to find the field, or alternatively rotate the elements of Eq. [21] and add the new to the old, the second-degree ($m = 2$) terms in Eq. [21] vanish, as found experimentally by Glover et al (12), and we are left with:

$$\tilde{B}_p^{(+)} = \beta_1\left(\Omega_1 \frac{-i2\mu_0 b k_i^3}{3k_e} h_1^{(2)}(k_e b)\right)\left(U_{0,0} - \frac{U_{2,0}}{2}\right), \quad (34)$$

which, in the limit as the frequency tends to zero, once again goes to $2\mu_o/3b$ (cf. Eq. [24]), as it should. The second-degree terms are now in the counter-rotating B_1 field $\tilde{B}_p^{(-)}$ but a second-order term is still present. Figure 3b shows a simulated image in the xy plane of the rotating frame B_1 field of Eq. [34] at 64 MHz; it has total azimuthal symmetry and is quite homogeneous, although not perfectly so. However, Figs. 4 and 5 show the variation at higher frequencies for various conductivities, and it is clear that the field is now inherently inhomogeneous, albeit with azimuthal symmetry. From Fig. 1 it is also clear that the phase varies over the sample—a point of some importance to which we shall return later. Finally, from Eq. [34], Fig. 6 shows the variation with frequency of the rotating frame B_1 field strength at the origin for constant current in the probe. It is very clear that there is a resonance phenomenon in the temporal sense that is damped by the sample's conductivity and to high accuracy ($<10^{-5}$) the resonance occurs when the diameter is an integral number of wavelengths. The relationship between the resonant frequency and sample diameter has been verified experimentally by the author. In the author's opinion, this phenomenon of "dielectric resonance" should be carefully distinguished from field focusing (Fig. 1). Resonance occurs at specific frequencies related to the size of the sample and its dielectric constant; field focusing occurs at all frequencies, becoming more pronounced and structured as frequency and/or dielectric constant increase(s). Both effects are diminished as conductivity increases.

RF Shimming

We are now in a position to evaluate power deposition and S/N, for we know the fields produced in the laboratory and rotating frames by unit current in a probe that is designed, at least at low frequency, to produce a homogeneous, circularly polarized B_1 field. Furthermore, the mathematical techniques developed are capable of describing in spherical Bessel harmonics the fields produced at high frequency by any distribution of magnetic moments and therefore current, on the surface of a spherical probe. The analysis could also be extended to probes on cylinders in analogy with the design of shim coils (19). However, the interesting question arises as to whether the inverse problem can be solved where, with appropriate probe design, it is possible to "shim out" the inhomogeneity in the B_1 field at high frequency, or to create a specific field profile. Unfortunately, we shall see that it is only possible to create a homogenous field (the "target field" in the following calculation) over certain surfaces within the sample and even then, the needed current distribution will be frequency and sample dependent. To proceed, we generalize our earlier procedure and first find the fields produced in the rotating frame by any order of surface harmonic distribution of magnetic moments on the surface of the probe sphere of radius b. We shall then specify an expansion of the field inside the sample, up to the order required to give a satisfactory fit to the target field. Finally, working in reverse, we shall find the amplitudes of the surface harmonics that produce these fields. In general, if we specify the field in the sample to order n, an extra field of order $n+2$ will be generated, but if n is sufficiently large, this extra term will have negligible impact.

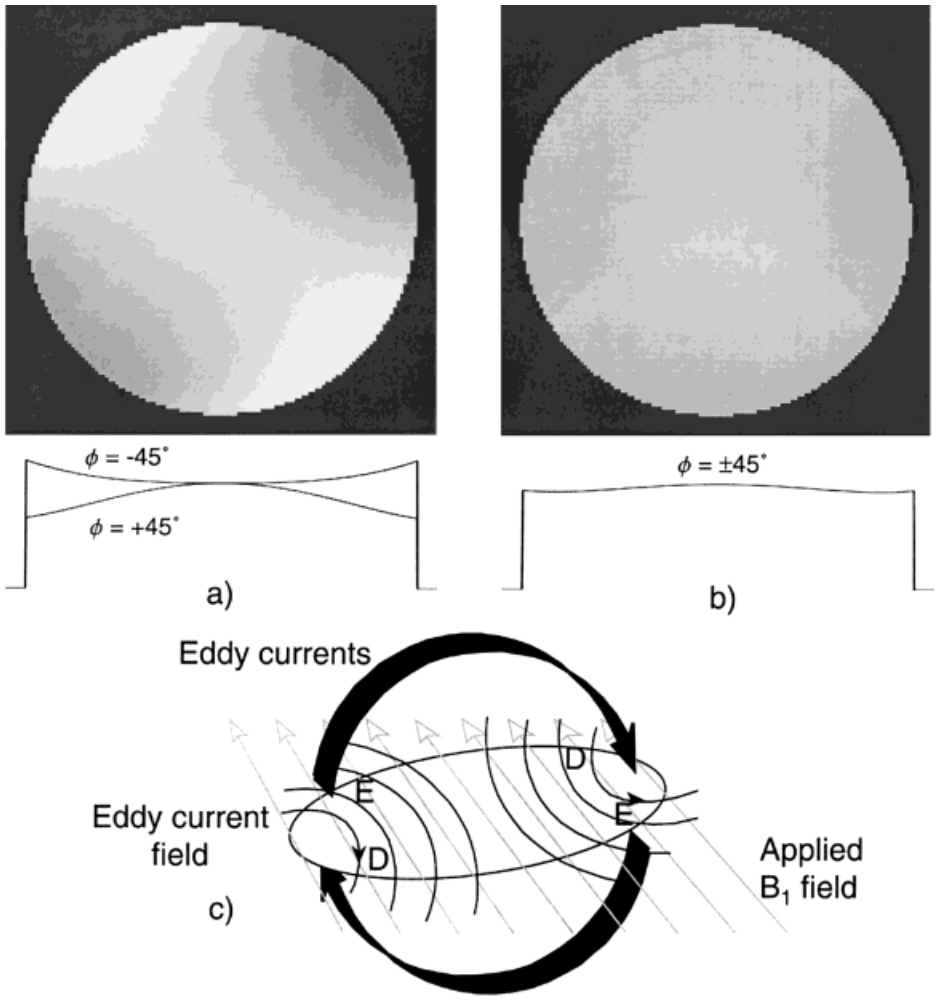

Figure 3. Simulated equatorial, transverse (*xy* plane) images of the rotating frame B_1 field (and therefore, neglecting symmetry considerations discussed in the text, approximately signal) strength in a spherical saline sample in a field of 1.5 T (64 MHz). The sample had a radius of 10 cm, with conductivity 1 Sm^{-1}. In **a,** the applied B_1 field was homogeneous and linearly polarized (ordinary probe), and we can see quite clearly that there are intensity variations from quadrant to quadrant. (The field amplitude plots are along the image diagonals.) Thus even at this relatively low frequency, the plot of Fig. 1 cannot be correct as it has only a radial variation—additional higher order terms ($U_{2,2}$ and $V_{2,2}$) are needed to describe the field correctly. This effect was first seen by Glover et al. (12). It can be understood by realizing that as the sample is mainly resistive at low frequency, the RF eddy currents, which flow in a polar orbit, as shown in **c,** have a phase that is toward being 90° different from that of the applied B_1 field. Now the eddy currents generate fields of their own. However, unlike the applied field, these eddy current fields are inhomogeneous and, in the midst of each quadrant, are almost perpendicular to the applied field. The combination of partial orthogonality of direction and partial orthogonality of phase in two fields (cf. a quadrature probe) is a recipe for major changes of field strength in the rotating frame. Thus, at points D, the field in the counterrotating frame is enhanced and the corotating frame field is diminished, while at points E, the opposite is true. It is interesting to note that the handedness of the NMR system destroys the mirror symmetry inherent in the physics of the laboratory frame fields. The higher order terms that describe the asymmetry are annulled when a circularly polarized field (quadrature probe) is applied, as seen in **b,** but the field is still radially slightly inhomogeneous, as we would expect from Fig. 1.

We begin by noting that an azimuthal distribution of elementary magnetic moments $d\mathfrak{m}$ as $\exp(-i\psi)$ on the surface of the sphere of radius b will always eradicate tesseral ($m \neq 0$) harmonics in the rotating frame field, a case in point being the quadrature arrangement described in the previous section. If we therefore assume that the distribution of elementary current loops over the surface of the sphere is given by a sum of surface harmonics of degree $m = 1$:

$$d\mathfrak{m} = \sum_{q=1}^{n_{\max}} \Omega_q P_{q,1}(\cos\,\alpha)\exp(-i\psi)b^2 \sin\,\alpha\; d\psi d\alpha, \quad (35)$$

where q is an integer and the Ω_q are constants, then from Eq. [17], the Hertz potential of the probe becomes:

$$\mathbf{\Pi}_p = \sum_{n=1}^{n_{\max}} C_n \left[iU_{n,0},\; U_{n,0},\; -2i\,\frac{(n-1)!}{(n+1)!}\,(U_{n,1} - iV_{n,1}) \right]$$

$$+ \sum_{n=2}^{\infty} C_n \frac{(n-1)!}{(n+1)!}$$

$$\times\,[i(U_{n,2} - iV_{n,2}),\; -(U_{n,2} - iV_{n,2}),\; 0], \quad (36)$$

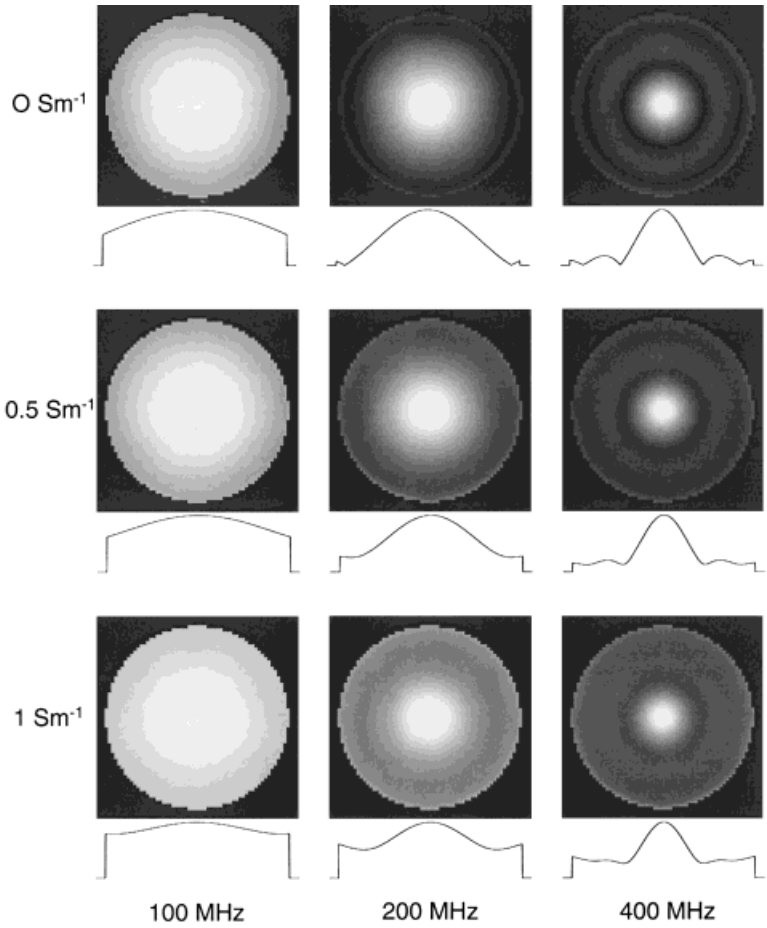

Figure 4. Simulated quadrature probe images of the B_1 field (and therefore approximately signal) strength in an equatorial, transverse (xy plane) section of a spherical saline sample, dielectric constant 80, at several conductivities and frequencies. The sample radius was 10 cm and all images are normalized to the same intensity at the center (see Fig. 6). The applied B_1 field in vacuo was as homogeneous as possible and was also circularly polarized. Thus there is no left-right asymmetry to be seen. In the first row, which is for pure water, there is very strong field-focusing, and at 400 MHz it is quite clear that there is almost a standing wave, as two black rings, indicating nodes in the field, can be seen. However, as the conductivity increases, this effect is clearly dampened, in accord with the plot of Fig. 1. The plots beneath each image are of field strength versus radius. To obtain an impression of how the B_1 field varies in a 10-cm radius sphere with a dielectric constant ϵ and conductivity σ Sm^{-1} at a frequency ν MHz, calculate frequency $\nu' = 0.11\nu\sqrt{\epsilon}$ and conductivity $\sigma' = 8.9\sigma/\sqrt{\epsilon}$. In this and all other figures, finding values, plots, or images that most closely correspond in frequency and conductivity to these new values gives the desired information.

where:

$$C_n = \frac{\omega_0\mu_0 b}{4k_e}(2n+1)h_n^{(2)}(k_e b) \times \left(\int_0^{\pi}\sum_{q=1}^{n_{max}} \Omega_q P_{q,1}(\cos\alpha)P_{n,1}(\cos\alpha)\sin\alpha\, d\alpha\right) = \frac{\omega_0\mu_0 b}{2k_e} n(n+1)h_n^{(2)}(k_e b)\Omega_n. \quad (37)$$

Note that a surface distribution of order n creates a potential of order n and that the second part of Eq. [36], with degree $m = 2$, produces a magnetic field in the z direction that does not contribute to the rotating frame B_1 field. Once again equating tangential electric and all magnetic fields at the surface of the saline sphere, we find that each order of Hertz basis vector is homologous across the boundary and that their internal amplitudes F_n are related to the driving amplitudes C_n by:

$$F_n = \frac{k_e^3(h_{n+1}^{(2)}(k_e a)j_n(k_e a) - h_n^{(2)}(k_e a)j_{n+1}(k_e a))}{k_i^2(k_e h_{n+1}^{(2)}(k_e a)j_n(k_i a) - k_i h_n^{(2)}(k_e a)j_{n+1}(k_i a))} C_n \equiv \beta_n C_n. \quad (38)$$

Note that for $n = 1$, Eq. [38] can be shown to be identical to Eq. [25] by application of Identity [27]. It follows from Eqs. [8] and [36] that the positively rotating frame field *in the sample* is:

$$\tilde{B}_p^{(+)} = \sum_{n=1}^{n_{max}} L_n((n+1)U_{n-1,0} - nU_{n+1,0}), \quad (39)$$

where constant L_n is given by:

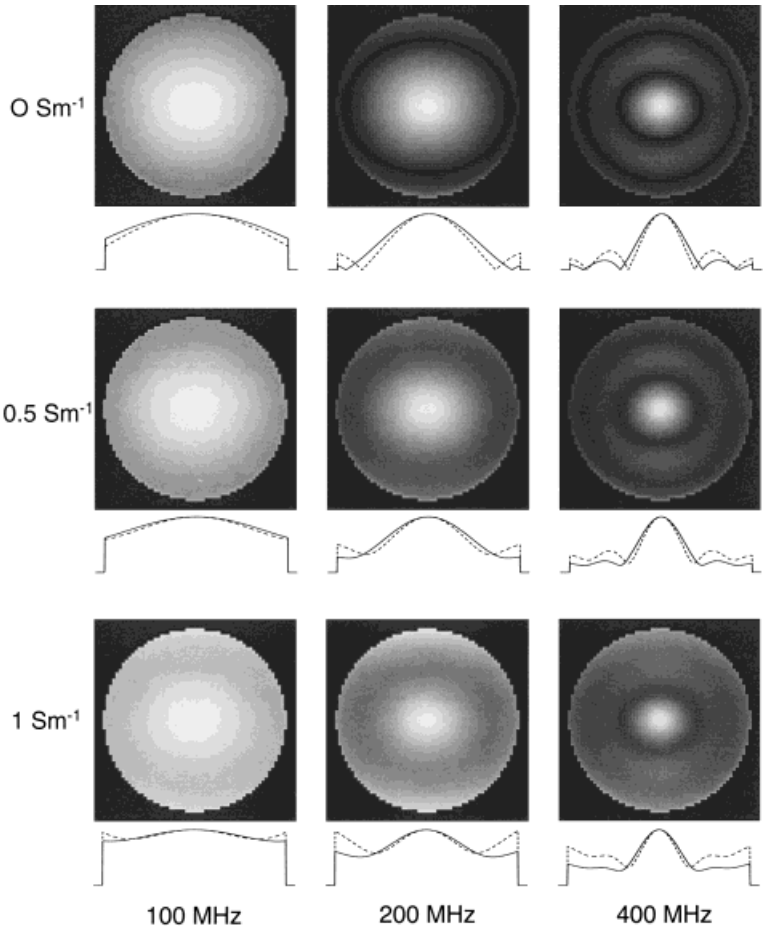

Figure 5. Simulated quadrature probe polar, coronal (*xz* plane) images of the B_1 field strength in a spherical saline sample at several conductivities and frequencies for the conditions given in Fig. 4. The influence of a second-order harmonic that is negligible in vacuo, but not so in the sample, causes the field strength to have a component that varies with declination as cos 2θ (see Fig. 2), and this can be clearly seen in the slightly elliptical nature of the image brightness. This effect is not seen in Fig. 4 because θ is constant at 90° for all images there. The plots beneath each image are of field strengths on the *x* (solid line) and *z* (broken line) axes (θ = 90° and 0°, respectively) and clearly show the range of the second-order field. The effect can again be understood by considering the eddy currents induced in the sample, although this time (eg, at 200 MHz for pure water), the displacement current may be dominant. With a circularly polarized applied B_1 field, the eddy currents cross paths at the sample's north and south poles, and the concentration of current there changes the field more markedly than at other declinations having the same radius. What the change actually *is* depends, of course, on sample composition and frequency.

$$L_n = \left(\frac{-ik_i^3}{(2n+1)\omega_0}\right)F_n = -\frac{i\mu_0 b k_i^3 n(n+1)}{2(2n+1)k_e}$$

$$h_n^{(2)}(k_e b)\beta_n\Omega_n. \quad (40)$$

Thus, taking liberties with the index n and introducing yet another constant for brevity, from Eq. [39] the coefficient K_n of the rotating frame field harmonic $U_{n,O}$ is $K_n = (n+2)L_{n+1} - \varsigma_n(n\text{-}1)L_{n-1}$ where ς_n is zero if $n = 0$ and one otherwise. We may now write a simple matrix equation, having in general two non-zero elements per row, linking the coefficients K_n with the amplitudes Ω_n of the magnetic moment surface harmonics. If we know the former, then the latter are easily obtained by matrix inversion. Alternatively, working from the lowest order up, a ladder procedure may be used to find the amplitudes.

Turning to the expansion of the target rotating frame magnetic field in spherical Bessel harmonics, as the functions $U_{n,O}$ are orthogonal over the surface of the sphere of radius a and form a basis set for the B_1 field, we may find the coefficients K_n of any desired field by finding its projection on that field basis set. However, it is immediately apparent that when the desired field is homogeneous, ie, constant, the only basis function that has a non-zero projection of a constant is $U_{0,O}$, and this function is, unfortunately, inhomogeneous. (Remember that the projection of a constant on the surface harmonic portion of the spherical Bessel harmonics is zero apart from $n = m = 0$.) It therefore would appear to be impossible *at high frequencies* to generate a homogeneous rotating frame field over the entire sphere—such a field is not a viable solution of Maxwell's equations, regardless of the coordinate system used. This statement may be verified by reference to the Helmholtz equation [6], which can only be satisfied for constant Ξ when $k = 0$, ie, at zero frequency. That having been said, it *is* possible, to high accuracy, either to remove

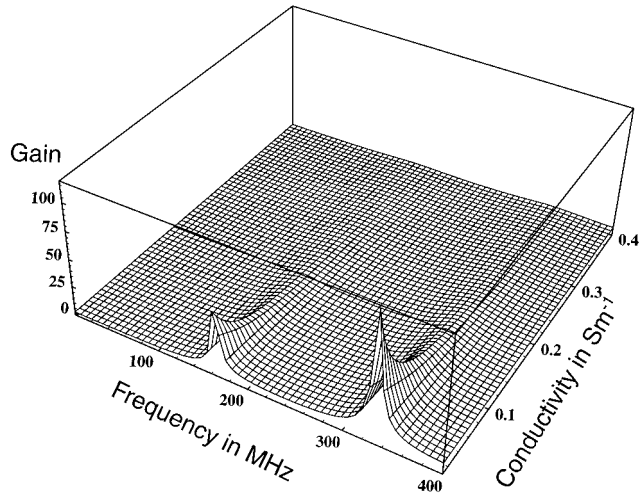

Figure 6. Enhancement of B_1 field strength at the origin with a quadrature probe as a function of frequency and sample conductivity. The radius of the sample is again 10 cm. So far, all the simulated images in the figures have been normalized to have the same intensity at the origin—the centers of the images. A sphere of water is essentially a cavity with standing waves being made possible at specific frequencies by reflection at the sphere's surface. A high degree of reflection takes place because of the disparity in dielectric constants within (~80) and without (1.0), resonance occurring when the diameter is an integral number of wavelengths in the sample. At a resonant frequency, there is large enhancement of the field at the origin—so-called dielectric resonance, but, as may be seen, it is damped when the sample has appreciable conductivity.

$U_{2,0}$ from the quadrature probe field of Eq. [34] or to generate a homogeneous field over certain surfaces and planes. For the first situation, we simply solve the matrix equation for as many values of $K_n = 0$ (apart from $K_0 = 1$) as is deemed necessary. We will be left with a field that is zeroth order plus a spurious and small final, high-order term. The required distribution of magnetic moments on the surface of the sphere of radius b is shown in Fig. 7 for various conductivities and frequencies, and the ensuing probe may be considered to be a phased array of Hertzian loops distributed over the surface of the sphere. Note the extreme behavior about a dielectric resonance.

An example for the second situation concerns the field in the transverse plane. It is clear from Eq. [13] that the field in the rotating frame $\tilde{x}\tilde{y}$ plane may be expressed as:

$$\underset{\text{sample}}{\tilde{B}_1^{(+)}} = \sum_{n=0}^{n_{\max}} K_n P_n(0) j_n(k_i r). \qquad (41)$$

Thus a simple computer fitting procedure can give the values of the K_n needed to create a field that is the best fit to a constant value. Figure 8 shows, for a saline sphere of unit conductivity at a frequency of 400 MHz, a plot of B_1 field versus declination and radius. The field in the transverse plane ($\theta = 90°$) has been rendered constant (<1% error) by a fit to sixth order, but it is clear that outside that plane, the field is highly inhomogeneous. Of course, for different frequency, conductivity, and permittivity, the plot will be different. The required distribution of magnetic moments or current loops on the surface of the outer sphere is also shown for an azimuth of $\psi = 0°$. (Remember, however, that the phase of the current loops also changes with azimuth as $-\psi$). Lest the reader think that the author is advocating the construction of probes on a sphere surrounding the patient, let me emphasize that this is not so; the above is only a mathematical exercise designed to demonstrate that it is possible to counteract, to a limited extent, field inhomogeneities caused by the electrical characteristics of the sample and the finite speed of light therein. Similar mathematics can be constructed for currents on the surface of a cylinder—it is just more complicated and this article is sufficiently difficult already! Thus the author envisages the day when ultra-high-frequency probes are optimized for the desired view within a volume.

Power Deposition

Having digressed to discuss inhomogeneity, let us return to Eq. [33], the Hertz basis vector for a circularly polarized, magnetic field that is homogeneous at low frequency in the rotating frame. The electric field created in the sample is immediately accessible from this equation via Eq. [10] but missing is the Hertz vector's amplitude. In practice, this is set experimentally by the user, by the expedient of selecting the desired value of *magnetic* field—for example, we may wish to generate a 90° pulse. Now at low frequency, we may assume a homogeneous B_1 field, but at high frequency, we have seen that we can no longer make this assumption and therefore there is a problem of definition. For example, we could define the *average* B_1 field over the sample and use that as a basis for setting the 90° pulse amplitude, or we could use the root mean square value, or the field that gives the largest FID, etc. It is strongly emphasized that different assumptions will give different results and in particular, it will be shown below that the size of an FID can be a very unreliable guide. For mathematical convenience, therefore, we shall assume throughout the rest of this article that the amplitude of the B_1 field in the rotating frame is defined *at the origin* with an amplitude there of $\tilde{B}_1^{(o)}$. (However, we include a factor ζ that allows for a different definition, if needed). Hence the electric field in the sample is given by:

$$\mathbf{E}_1^{(i)} = \frac{3\omega_0 i\zeta \tilde{B}_1^{(o)}}{2k_i}\left[U_{1,0},\ -iU_{1,0},\ -(U_{1,1} - iV_{1,1})\right], \qquad (42)$$

and the power deposited in an elementary volume dV, remembering that $\mathbf{E}_1^{(i)}$ is an amplitude, is:

$$dW = \mathbf{E}_1^{(i)} \cdot \mathbf{E}_1^{(i)*} \frac{\sigma}{2}\, dV. \qquad (43)$$

Computed images of this function, which is a measure of the specific absorption rate (SAR), are shown in Fig. 9 for various frequencies and conductivities; it may be seen that, whereas at low frequencies, the maximum

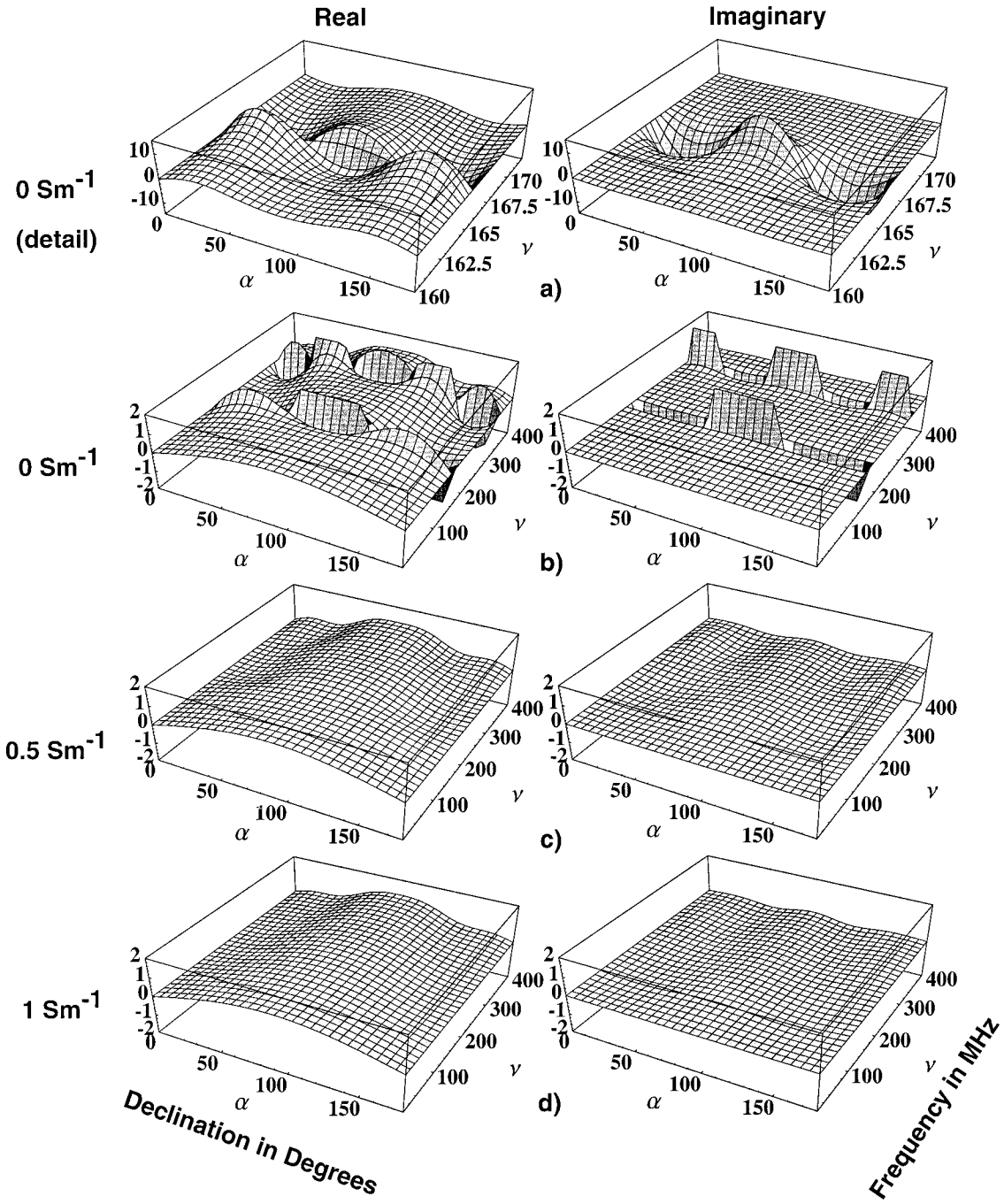

Figure 7. The distribution, as a function of declination α in degrees and frequency ν in MHz, of the radiofrequency magnetic moments on the surface of the outer sphere of Fig. 2 (the "probe" sphere), needed to keep the field in the sample as homogeneous as possible by generating only the lowest order term ($U_{0,0}$ to the sixth order) in the expansion of the field. With reference to Fig. 1, however, the homogeneity at high frequency is still awful, and it is not possible to generate a homogeneous field—it is not a solution of Maxwell's equations. The azimuthal distribution is not shown because it always multiplies the plots by the same function $\exp(-i\psi)$ to create a circularly polarized field. Plots for three different sample conductivities are shown; the first plot (**a**) is a detail from the second plot (**b**), both for pure water, showing the great swings in the distribution function (note the vertical scales) in the region of a dielectric resonance. When we look at plots **c** and **d,** while a third-order variation is still just visible about resonance, the wild excursions in these regions have been greatly dampened by the conductivity of the sample, and the plots are seen to ride on a first-order base—a real variation as sin α, which is what is required with a spherical probe at low frequencies to create a truly homogeneous field. This can best be seen in the real parts of plots c and d at 0 Hz.

SAR is at the surface of the sphere, this is no longer true at higher frequencies. Now the human head has good heat removal mechanisms for its surface, apart from the eyes, but not for its interior. Thus caution should be exercised when imaging at high frequency, assuming that a head behaves like a conducting, high-permittivity sphere. The images of Fig. 9 give, of course, no indication of the *absolute* power absorbed, so Fig. 10a

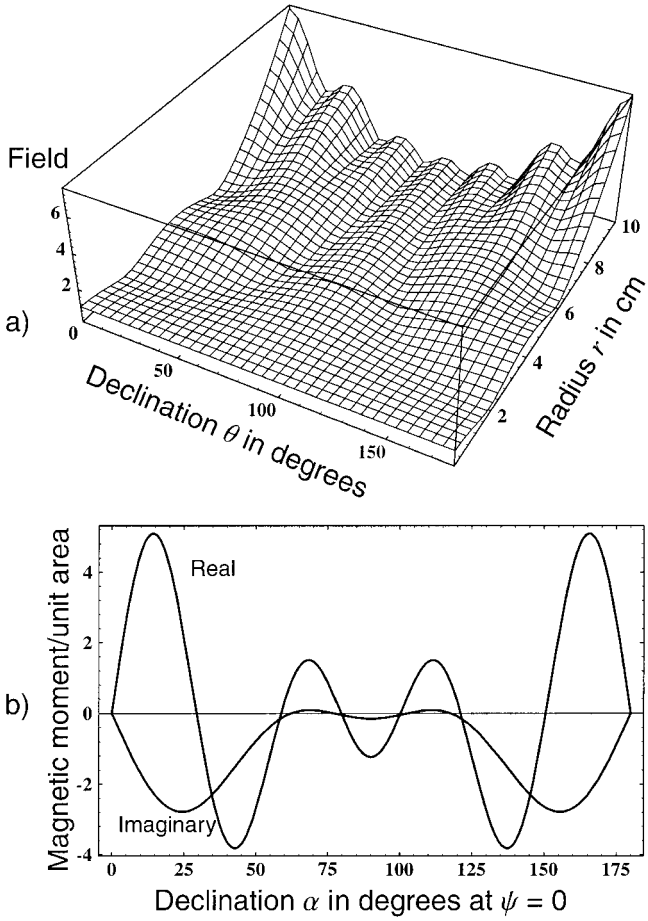

Figure 8. **a:** The rotating frame B_1 field variation in the sample with declination θ and radius r is shown for a distribution of magnetic moments on the outer sphere that aims, to the sixth order, to create within the sample a homogeneous field in the *xy* plane (θ = 90°). Any attempt to obtain perfect homogeneity at high frequency over the entire sample is doomed to failure because a homogeneous field is not a solution of Maxwell's equations. However, it is possible to create a field that is homogeneous over certain surfaces, and it may be seen that for θ = 90°, there is negligible change in amplitude with radius. **b:** How the distribution of magnetic moments on the surface of the probe sphere varies in amplitude and phase with declination α at azimuth ψ = 0. Of course, it only needs the sample conductivity or size to change, let alone the Larmor frequency, and a new distribution is needed. Nevertheless, a probe for the "average" patient could be designed for a specific B_0 field. If the quadrature hybrid, or other device used for ensuring excellence of field orthonormality in transmission and reception, is tampered with, and the pulse flip angle is adjusted, it is possible, at least in simulations, to improve apparent *image* homogeneity at the expense of signal-to-noise ratio. While interesting, this digression is not pursued here.

shows the SAR (σ = 1 Sm^{-1}), for a constant B_1 field at the origin, plotted as a function of frequency and distance along the z axis. The latter variable was chosen because, as may be seen in Fig. 9, the power deposition is greatest there. It is perhaps surprising that the maximum SAR *decreases* a little with increasing frequency (follow the ridge in the figure) once the "hot" region moves into the sample's interior.

Integrating over the sphere to find the total power deposited, we have that:

$$W = \int_0^a \frac{6\pi\sigma}{k_i k_i^*} (\zeta \tilde{B}_1^{(o)} \omega_0 r)^2 j_1(k_i r) j_1^*(k_i r)\, dr, \qquad (44)$$

and at low frequency, setting ζ = 1, as $j_1(k_i r) \approx k_i r/3$:

$$W = \frac{2\pi\omega_0^2 \tilde{B}_0^2 a^5 \sigma}{15}, \qquad (45)$$

which, as it should be, is twice the formula for a *linear* probe given by Hoult and Lauterbur (2). Figure 10b shows how the RF power required for a 90° pulse *at the origin* deviates at high frequency from the value presented by the "traditional" formula, Eq. [45], as the radius a of the sample increases. In other words, when the sample is sufficiently large, the power required is less than one would predict from near-field formulae with their quadratic dependence, as is well known (1,7). (The conductivity of the sample is unity.) We plot the ratio of Eqs. [44] and [45], as it is independent of the pulse length and type, and the "traditional" formula is often used to obtain a rough assessment of required power. Furthermore, the dynamic range of the plot is greatly reduced, resulting in a clearer display. An intuitive understanding of this phenomenon may be obtained by realizing that the voltage induced in a ring of conductor in the sample is dependent on the flux linkage through the ring. However, at high frequency, the phase of the B_1 field changes with radius and so the total flux linkage does not increase as rapidly as one might expect. Thus the total power deposited is lowered.

Signal-to-Noise Ratio

We are now finally in a position to assess the intrinsic S/N of the sample (11). We shall not attempt to assess degradations of S/N from radiative or resistive losses in the probe, nor from radiative loss into regions of the sample remote from the probe and from the sample into space. Radiative losses into space should be rendered negligible by good engineering practices—from the probe by appropriate shielding and from the patient or sample by appropriate probe electrical balancing and shielding. The resistive losses in probes are usually negligible in comparison with those in the sample. To calculate the voltage induced, by a rotating nuclear magnetic moment at point P(r,θ,ϕ) in the sample, in elementary conducting loops on the surface of the sphere of radius b, we use the Principle of Reciprocity (2,26,27). Doubt has been cast (8) on the validity of the Principle of Reciprocity for the calculation of magnetic resonance signal strength and noise. However, the Principle is a fundamental consequence of causality (21,24) and can be shown to apply rigorously, the usual expression thereof being a corollary of Green's theorem. It is, however, a principle that is valid in the *laboratory* frame and may not be expected to hold in a rotating frame where the symmetries inherent in its derivation have been violated by the imposition of handedness. A

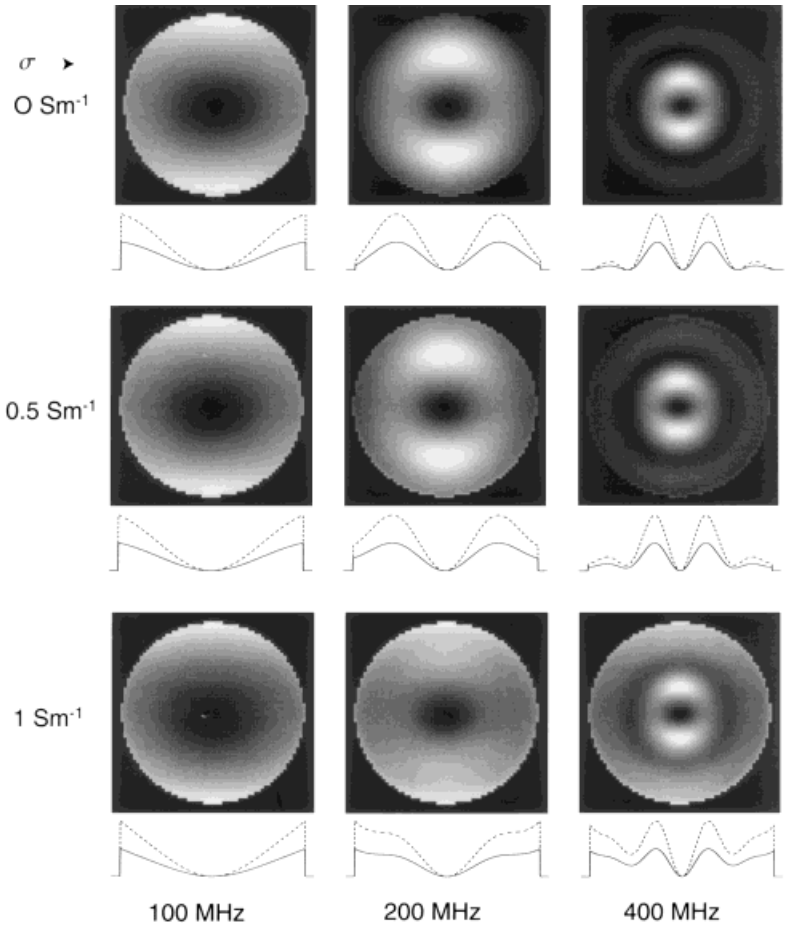

Figure 9. Simulated quadrature probe polar, coronal (*xz* plane) images of the normalized specific absorption rate (SAR) in a spherical saline sample at several conductivities and frequencies for the conditions given in Fig. 4. Plots are along the *x* (solid line) and *z* (broken line) axes. Previous images have been of the rotating frame magnetic field generated in the sample; these are of EE^*, the square of the electric field *E*, as SAR is proportional to this quantity. Note how at low frequency, as is well known, the power deposition is a maximum on the edge of the sample and is greatest at the poles where radiofrequency eddy currents, associated with the two quadrature B_1 fields, converge. The human body is adept at removing heat from the its exterior, apart from the eyes, so in a normal individual at low frequency, SARs of the order of watts per kilogram are well tolerated. However, as the frequency increases, the region of maximum SAR moves inside the saline sample. If this effect also occurs in the head, caution is indicated as heat removal mechanisms are minimal in the brain. The spatially periodic nature of the power deposition is clearly visible, particularly in the plot at 400 MHz and 1 Sm^{-1}.

full description of the high-frequency use of the Principle is given in ref. 28. There it is shown that if magnetization is described in a positively rotating frame as resulting from the transmitter $\tilde{B}_{1T}^{(+)}$ field in that frame, then the received signal is proportional to the complex conjugate of the field in the *negatively* rotating frame $\tilde{B}_{1R}^{(-)*}$ due to unit currents, provided that field is calculated for those currents *with the phase shifts appropriate for signal reception*. The derivation of such a field follows from Eq. [20] in a manner similar to that employed for Eq. [34], and it may be shown that for our spherical sample, that field is also described by Eq. [34] for unit current. However, the reader is cautioned that in general, the two fields $\hat{B}_{1T}^{(+)}$ and $\hat{B}_{1R}^{(-)*}$ are not necessarily equal.

In thinking about how the concept of unit current melds with that of a probe comprising a nonlinear distribution of magnetic moments on the surface of a sphere, it may be helpful to consider that the various strengths of the elementary magnetic moments implicit in Eq. [21] are determined by their elemental area and/or number of turns so that the concept of unit current can be retained. However, we shall see below, as is well known, that the concept is not vital if we are only calculating intrinsic S/N. Following Eq. [34], if $\tilde{M}_{xy}^{(+)}$ is the component of nuclear magnetization in the positively rotating $\tilde{x}\tilde{y}$ plane, the initial amplitude of the received free induction decay (FID) is given by:

$$d\xi(r,\,\theta) = \tilde{M}_{xy}^{(+)}(r,\,\theta)dV\omega_0\hat{B}_1^{(o)}(U_{0,0}(r,\,\theta) - 0.5U_{2,0}(r,\,\theta)). \quad (46)$$

The spatial dependencies have been explicitly indicated, and a homogeneous main B_0 field is assumed. Note in particular that as the transmitting B_1 field is inhomogeneous, we have *not* assumed that $\tilde{M}_{xy}^{(+)}$ is equal to the equilibrium magnetization M_0. On the contrary,

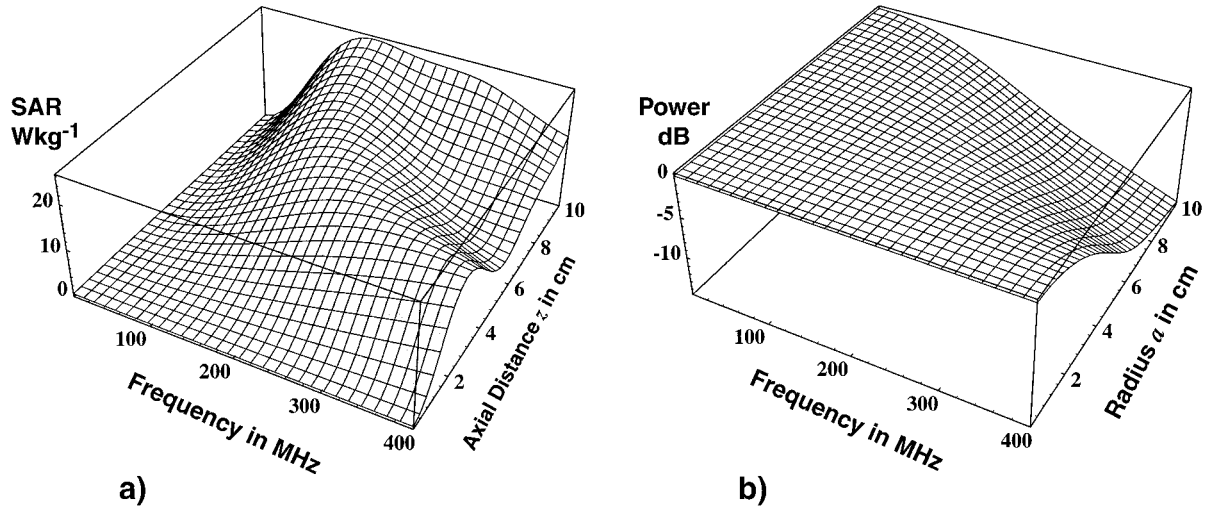

Figure 10. **a:** The absolute SAR, for an applied B_1 field from a quadrature probe of 5.87 μT ($\nu_1 = 250$ Hz) at the origin in the rotating frame, as a function of frequency, and distance along the z axis where power deposition is greatest (Fig. 9). The sample has unit conductivity and a radius of 10 cm. The plot shows clearly that at any particular value of z, the SAR passes though a maximum with increasing frequency and then diminishes. This is entirely due to the fact that the wavelength *in the sample* becomes comparable to or less than the sample radius. However, what is not quite so easily visualized is that the ridge in the plot gently diminishes in height as we follow it from {200 MHz, 10 cm} to {400 MHz, 3 cm}. **b:** We are allowing the size of the spherical sample to vary (N.B.), and are plotting the total power (ie, the required transmitter power) absorbed by a sample of unit conductivity as a function of frequency and sample radius. This is the first plot where it is not directly the dependent variable that is plotted, but rather a ratio to reduce the dynamic range. Thus the power needed is compared with the value predicted by the "traditional" low-frequency formula of Hoult and Lauterbur (2), which has a quadratic dependence on frequency and a fifth-power dependence on sample radius. In the plot, it is quite clear that at higher frequencies somewhat less power is needed than might be expected (up to −14 dB or a factor of 5). We see in Fig. 9 that there are nodal regions in the sample where the electric field is small and hence the power deposition there is small too. When we integrate over the sphere to find the total power, these nodal regions reduce the sum. In turn, by reciprocity, Nyquist's famous formula predicts that the received noise will be lower than expected.

for a simple, nonadiabatic pulse, the flip angle across the sample will vary greatly at high frequency both in amplitude and phase, and for a small (<10°) flip angle at the origin, the signal will be proportional to the square of the term in parentheses—see below. At low frequency, Eq. [46] reduces to the expression of Hoult and Richards (26), albeit for a *quadrature* probe:

$$d\xi = \tilde{M}_{xy}^{(+)} dV \omega_0 \hat{B}_1^{(o)} \qquad [47]$$

Turning to the calculation of the noise, the Principle of Reciprocity concerning *electric* fields must also apply to the reception of electric dipole Brownian noise from the sample and hence, from Eq. [44], if we set $\tilde{B}_1^{(o)} = \hat{B}_1^{(o)}$, we may equate the power W with an effective resistance $r_m/2$. The noise is then given by Nyquist's equation $N = (4\kappa T r_m \Delta\nu)^{1/2}$ and from Eq. [46], the intrinsic volume element free induction decay S/N ratio $d\Psi$ is:

$$d\Psi = \tilde{M}_{xy}^{(+)} dV (U_{0,0} - 0.5 U_{2,0}) \times \left(\frac{12\pi\sigma\kappa T\Delta\nu}{k_i k_i^*} \int_0^a r^2 j_1(k_i r) j_1^*(k_i r) dr \right)^{-1/2} \qquad [48]$$

where κ is Boltzmann's constant, T is the sample temperature, and $\Delta\nu$ is the bandwidth of the receiver. Note that there is no dependence on $\hat{B}_1^{(o)}$ the strength of the B_1 field at the origin, and hence unit current in the coils is a conceptual convenience here. At low frequencies, from Eqs. [45] and [47], this reduces to:

$$d\Psi = \tilde{M}_{xy}^{(+)} dV \left(\frac{4\pi\sigma\kappa T a^5 \Delta\nu}{15} \right)^{-1/2}, \qquad [49]$$

which is root two times the formula quoted by Chen and Hoult (14) for a *linear* probe. Readers may convince themselves with two lines of algebra that the ratio of Eq. [48] to [49] *at the sample origin* is just the inverted plot of Fig. 10b, and as that plot is conveniently in decibels ($20 \log_{10}$[ratio]), the desired ratio may be obtained from it simply by negating the vertical scale. In other words, the relative volume element S/N at the origin *increases* as a function of frequency and sample radius a, compared with the value expected from the traditional formulation, Eq. [49], and if an adiabatic 90° pulse has been employed so that $\tilde{M}_{xy}^{(+)} = M_0$ throughout the sample, then Figs. 4 and 5 may be used as a guide as to how the S/N varies across the field of view. Because the volume element S/N varies widely at high frequency across the sample and is dependent on the method of excitation, careful definition is essential. For example, if an ordinary pulse were used, the spatial variation would be more dramatic, but note that a large (>90°) flip angle at the origin can smooth some of the variation, as can missettings of the quadrature hybrid assumed to be used with any probe. Figure 11 shows three representative plots of the variation of the average S/N in

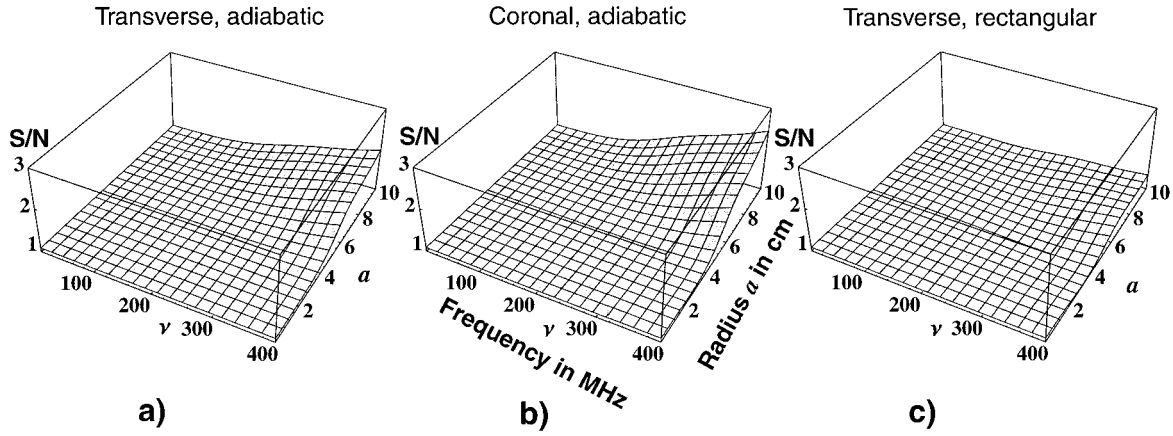

Figure 11. Plots of root mean square signal-to-noise ratio in an imaging plane versus frequency and sample radius a. Note that the size of the sample is being varied. The S/N is averaged over the whole plane and again, it is a ratio that is plotted to reduce dynamic range. The S/N is being compared with that predicted by the traditional formula of Hoult and Lauterbur (2). **a:** For a transverse equatorial (xy plane) section. **b:** For a coronal polar section (xz plane). In both plots, an adiabatic 90° pulse was presumed to have been used so that the flip angle was the same at all points in the sample. **c:** For a transverse equatorial (xy plane) section; a simple rectangular or monophasic pulse was employed. In all three plots, the S/N averaged over the plane may be seen to be greater, to various degrees, at high frequencies than the value that would be predicted by the traditional formula, apart from in small regions in b and c at 400 MHz and a sample radius of 3 cm. Thanks to the spatial variation of B_1 field strength (see Fig. 1), the average absolute signal strength is lower than we might expect. However, the power deposition (see Fig. 10b) is even lower, and so on average, the S/N ratio is increased. It follows that when comparing the performances of disparate equipment, one must be very careful to specify the manner in which the S/N was measured and whether it was for a particular location, over a particular region or plane, etc., and what type of excitation was used. Manifestations of "specmanship"—the presentation of specifications in the best possible light while obscuring detail—are all too easy. No consideration has been given to the influence of variables such as chemical shift range and relaxation times on image sensitivity.

imaging planes with frequency and sample size for unit sample conductivity; the general form of such plots is similar for lower conductivities.

Once again, the plots are relative to the "traditional" formula to minimize dynamic range and to make more obvious deviations from a linear frequency law. ($\tilde{M}_{xy}^{(+)}$ in Eq. [49] is proportional to frequency.) Thus in Fig. 11a, still using an adiabatic pulse, the root mean square (RMS) relative S/N for a transverse (xy) plane is shown, while Fig. 11b shows a similar plot for a coronal or sagittal section. Figure 11c is the transverse plot when using a simple monophasic rectangular or shaped pulse. In all cases, even though the plotted S/N is an average over the imaging plane, rather than being just at the origin, the relative S/N ratio is greater than that predicted by the traditional formula, apart from very small regions in Fig. 11b and c.

Taking a small digression, a definition of sensitivity more normally used in spectroscopy concerns the initial S/N of the FID from the *entire* sample in the absence of gradients; an interesting phenomenon occurs here that *reduces* that S/N. To find the FID amplitude, we must integrate Eq. [46] over the sample. However, to do so, we must once again know how $\tilde{M}_{xy}^{(+)}$ varies with spatial position. This depends on the details of the RF pulse. However, in all cases the pulse imparts to the magnetization at a particular volume element the phase of the driving B_1 field there. Now at low frequencies with a probe used for both transmission and reception, any rotating frame phase variation across the sample, caused by diverse directions of the B_1 field, is canceled at reception by an opposite phase variation. Mathematically, the transmitter field gives a positive rotating frame field that is $(B_x + iB_y)/2$ where B_x and B_y are real quantities, and thus the phase of the transverse magnetization $\tilde{M}_{xy}^{(+)}$ is determined by the argument of this quantity minus 90°. However (28), the received signal is proportional to $\tilde{M}_{xy}^{(+)}(\hat{B}_x - i\hat{B}_y)$ which implies an overall dependency as $\hat{B}_x^2 + \hat{B}_y^2$ and phase variations with spatial position therefore vanish—the received signals from the volume elements at different places add coherently. However, at high frequencies, we have both phase and directional changes caused by the conductivity and high dielectric constant of the sample. Thus $\hat{B}_x$ and $\hat{B}_y$ are in general complex and so is $\hat{B}_x^2 + \hat{B}_y^2$. If we now consider the effects of a pulse of small flip angle ϑ for mathematical simplicity, we may make the approximation that the $\tilde{x}\tilde{y}$ magnetization is given by $\tilde{M}_{xy}^{(+)} = M_0\vartheta(r,\theta)$. Thus, from Eq. [46], or by careful analysis from Eq. [21] and its y counterpart, the signal from the entire sample is:

$$\xi = \omega_0 M_0 \vartheta^{(o)} \hat{B}_1^{(o)} \int_{\text{sample}} (U_{0,0} - 0.5U_{2,0})^2 dV$$

$$= \omega_0 M_0 \vartheta^{(o)} \hat{B}_1^{(o)} \int_{\text{sample}} (U_{0,0}^2 + 0.25U_{2,0}^2) dV, \quad (50)$$

where $\vartheta^{(o)}$ is the flip angle at the origin. The S/N of the FID from the entire sample, compared with that expected from the traditional formula (again to reduce the dynamic range associated with a large frequency span), is plotted in Fig. 12 on a logarithmic scale as a function of frequency and conductivity; there are two "holes" of zero signal at frequencies of 178.05 and 355.82 MHz.

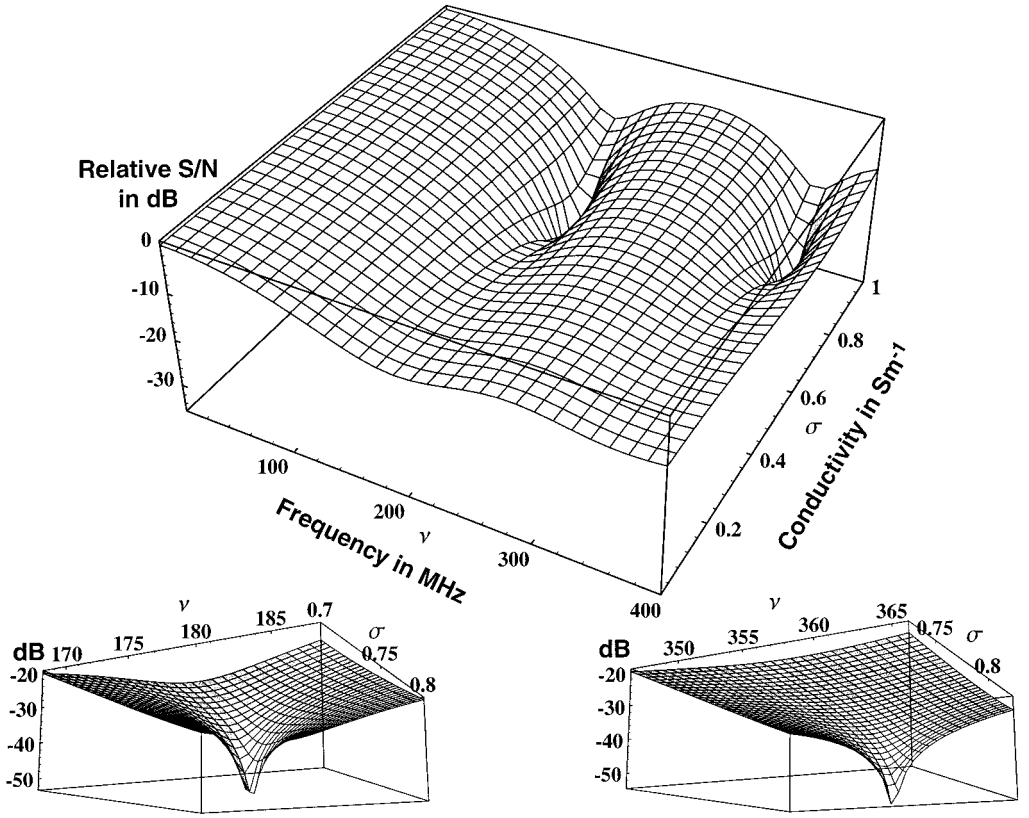

Figure 12. An intriguing prediction of the theory, applicable to spectroscopy. No gradients are being applied. The signal-to-noise ratio of the free induction decay *from an entire sample* of radius 10 cm as a function of frequency and conductivity is shown following a small flip angle pulse. Again, the S/N is compared with what one would expect from the theory of Hoult and Lauterbur (2), but a logarithmic scale is used as this gives the clearest picture. (The dynamic range *in the ratio* is a factor of 300 or −50 dB.) In general, the two values are comparable (0 dB), but at two places in the plot, there are deep "holes" in the response, and these are shown from below in the smaller figures. The reason for the holes is destructive interference when the signal from the entire sample is integrated. We have concentrated in most of the previous figures only on the *amplitudes* of variables, as it is these that tend to influence quantities of interest such as image quality and SAR. However, when we consider an integrated response over the entire sample, the phase of the signals from various regions becomes crucial (Fig. 1). These phase shifts add in a causal manner; they do not cancel as do phase shifts associated at low frequency with diverse directions of the B_1 field. Thus, for certain combinations of frequency and conductivity, it is possible to obtain a zero integral—a global node is produced.

We might expect such phenomena to occur at specific frequencies that are dependent on the size of the sample, but at first sight it seems odd that the needed conductivities are so specific. However, when we remember that it is the conductivities that are responsible for the position-dependent phase changes (k_i is real for zero conductivity, whence $U^2_{n,O}$ is always real and positive), it is not surprising that a specific value is implicated—the phase changes across the sample are then such that signals cancel. ($\angle k_i = -21.74°$ for a primary "hole.") The building of equipment to test this conclusion is currently under way. In an image, one does not see this behavior because one is not summing the signal over the sample; on the contrary, the whole point of the imaging experiment is to break the sample down into volume elements. However, if a phase-sensitive image were to be taken, the phase variations across the sample would easily be seen.

CONCLUSIONS

The performance of the NMR imaging experiment at high frequencies where the wavelength in the sample is comparable to or less than the latter's dimensions has been assessed. To that end, a rigorous and full solution of Maxwell's equations for a conducting sphere of high dielectric constant, subjected to an ostensibly homogeneous, B_1 field created by currents on a spherical probe outside the sphere, has been found. The effects of both linearly and circularly polarized driving fields have been calculated in both the laboratory and rotating frames. As circularly polarized fields were used, the simplifying technique of employing axial symmetry (B_1 field in the z direction) could not be employed, and tesseral harmonics, with their attendant difficulties, were used. The framework of the solution is in a format (the Hertz vector) that can be expanded at a later date to accommodate the fields created by probes with appreciable charge separation in their conductors.

From the electric field solutions in the laboratory frame, the power deposited in the experiment has been calculated, and, employing the Principle of Reciprocity, the S/N has also been found. The author is not so sanguine as to believe that no errors, typographical or otherwise, have crept into a complex paper that summarizes 50 pages of mathematics and would appreciate notification of any

errors readers may detect. However, the results seem to be in accord with known phenomena such as dielectric resonance and field focusing, and they make intuitive sense. Unfortunately, the author, at the time of writing, is not in a position to test the predictions of the theory fully. Furthermore, it must be reiterated that the head is a complex object with a variety of conductivities and dielectric constants, and so exact correspondence with the results presented here is not to be expected (9,10). Nevertheless, the general trends revealed by the theory are pertinent and in accord with previous work. Summarizing, these are that at high frequency in a spherical sample of conductivity and size roughly approximating that of the human head:

1. The B_1 field in the rotating frame is inherently inhomogeneous, varying substantially with radius in amplitude and phase, and is strongest at the origin—the field focusing effect.
2. The current distribution in a probe that yields a homogeneous field at low frequency does not yield the most homogeneous field at high frequency.
3. A fully homogeneous field is not a solution of Maxwell's equations at high frequency. Thus the B_1 field cannot be rendered uniform over the entire sample, merely over certain surfaces such as the transverse plane. The distribution of RF current required to create such a partly homogeneous field is sample and frequency dependent.
4. Fields inside the sample are resonant when, to considerable accuracy, the diameter of the sample equals an integral number of wavelengths. Under such conditions, the B_1 field at the origin of a sample of pure water can be greatly increased, and such enhancement may have practical use for boosting sensitivity in some specialized experiments, in much the same way that ferrites can at low field strengths. The greater the sample conductivity, the more dampened is the resonance.
5. The power required for a 90° pulse *at the origin* is less than that predicted by the traditional formula of Hoult and Lauterbur (2). This result is in agreement with the predictions of Bottomley and Andrew and the observations of Robitaille et al.
6. The maximum SAR no longer occurs at the surface of the sample, but rather moves inside as the frequency increases and also thereafter decreases slightly. Note that the head has its main heat-removal mechanisms at the surface and thus caution should be exercised.
7. The intrinsic image volume-element SNR varies considerably over the sample but on average is usually slightly greater than the value predicted by Hoult and Lauterbur. The factor depends on the experimental details.
8. The bulk intrinsic SNR, as measured by the size of the FID in the absence of gradients, can show severe reduction, depending on frequency and sample conductivity, due to destructive interference caused by major changes of phase with radius in the sample. Thus the FID may not be a good indicator of flip angle.

ACKNOWLEDGMENTS

The author acknowledges useful discussions with M. Alexander, C.-N. Chen, C. Collins, H. Eviatar, I.C.P. Smith, M. Smith, R. Somorjai, and P. Unger. He also acknowledges useful comments and the provision of ref. 29 by the referees.

APPENDIX

Identities

The following identities are used, taken from the book by Abramowitz and Stegun (25), except for Identity [A6], which is from Erdelyi et al (29). For the associated Legendre polynomials, Ferrer's function (30) was employed, and thus considerable care is needed in using the identities in ref. 25. In general, their factor $(z^2 - 1)^{1/2}$ should be replaced by $-\sin\theta$, and there is also a factor of $(-1)^m$ difference.

For spherical Bessel functions of all types:

$$(2n + 1)\frac{d}{dr}f_n(r) = nf_{n-1}(r) - (n + 1)f_{n+1}(r), \quad \text{(A1)}$$

$$(2n + 1)\frac{f_n(r)}{r} = f_{n-1}(r) + f_{n+1}(r). \quad \text{(A2)}$$

For the associated Legendre polynomials, where $u = \cos\theta$:

$$P_{n,m}(0) = 2^{\left(\frac{m-n}{2}\right)} \times \cos\left((n - m)\frac{\pi}{2}\right)\frac{1\cdot 3\cdot 5\cdot 7\cdots(n + m - 1)}{\left(\frac{n-m}{2}\right)!} \quad \text{(A3)}$$

$$\sin^2\theta\,\frac{\partial}{\partial u}P_{n,m}(u) = (n + m)P_{n-1,m}(u) - nuP_{n,m}(u) \quad \text{(A4)}$$

$$(2n + 1)uP_{n,m}(u) = (n - m + 1)P_{n+1,m}(u) + (n + m)P_{n-1,m}(u) \quad \text{(A5)}$$

$$(n - m + 1)\sin\theta P_{n,m-1}(u) = uP_{n,m}(u) - P_{n-1,m}(u) \quad \text{(A6)}$$

$$-\sin\theta P_{n,m+1}(u) = (n - m)uP_{n,m}(u) - (n + m)P_{n-1,m}(u). \quad \text{(A7)}$$

Cartesian Differentiation of Spherical Bessel Harmonics

The function to be differentiated is:

$$\Xi = f_n(kr)P_{n,m}(\cos\theta)^{\cos m\phi}_{\sin m\phi}. \quad \text{(A8)}$$

The Cartesian differentials in spherical polar coordinates are:

$$\frac{d\Xi}{dx} = \sin\theta\cos\phi\,\frac{\partial\Xi}{\partial r} - \sin\theta\cos\theta\cos\phi\,\frac{1}{r}\frac{\partial\Xi}{\partial u} - \frac{\sin\phi}{r\cos\theta}\frac{\partial\Xi}{\partial\phi}$$

$$\frac{d\Xi}{dy} = \sin\theta\sin\phi\,\frac{\partial\Xi}{\partial r} - \sin\theta\cos\theta\sin\phi\,\frac{1}{r}\frac{\partial\Xi}{\partial u} + \frac{\cos\phi}{r\cos\theta}\frac{\partial\Xi}{\partial\phi}$$

$$\frac{d\Xi}{dz} = \cos\theta\,\frac{\partial\Xi}{\partial r} + \sin^2\theta\,\frac{1}{r}\frac{\partial\Xi}{\partial u}, \qquad \text{(A9)}$$

where $u = \cos\theta$, and, importantly, we know that the resultants must be sums of spherical Bessel harmonics, for the Helmholtz equation is obeyed by both a scalar potential and its Cartesian fields. We consider first, by way of example, the derivative in x of a $\cos m\phi$ spherical Bessel harmonic and inspect the terms in ϕ. They are of the form $\cos\phi\cos m\phi$ and $\sin\phi\sin m\phi$, and we immediately see that the degrees of the component harmonics are therefore $m-1$ and $m+1$. Thus the coefficients of the terms $\cos[(m-1)\phi]$ and $\cos[(m+1)\phi]$ are, in order plus, minus:

$$\frac{1}{2}\left[\sin\theta\,\frac{\partial}{\partial r}f_n(kr) \pm \frac{m}{\sin\theta}\frac{f_n(kr)}{r}\right]P_{n,m}(u) - \frac{\cos\theta\sin\theta}{2}\frac{f_n(kr)}{r}\frac{\partial}{\partial u}P_{n,m}(u). \qquad \text{(A10)}$$

Turning to the radial terms in Eq. [A9], we know that differentiation must reduce by one the order and that the parity of any extra higher orders generated must be the same as that of the base order. Thus we may expect terms of order $n-1$, $n+1$, $n+3$, etc. Applying Identities [A1] and [A2] to expression [A10], we have:

$$\frac{d\Xi}{dx} = \frac{k}{2(2n+1)} \times \left\{\begin{array}{l}\left[n\sin\theta \pm \dfrac{m}{\sin\theta}\right]P_{n,m}(u) \\ -\cos\theta\sin\theta\,\dfrac{\partial}{\partial u}P_{n,m}(u)\end{array}\right\} f_{n-1}(kr)\cos[(m\mp1)\phi]$$

$$+ \frac{k}{2(2n+1)} \times \left\{\begin{array}{l}\left[-(n+1)\sin\theta \pm \dfrac{m}{\sin\theta}\right]P_{n,m}(u) \\ -\cos\theta\sin\theta\,\dfrac{\partial}{\partial u}P_{n,m}\end{array}\right\}(u) f_{n+1}(kr)\cos[(m\mp1)\phi], \qquad \text{(A11)}$$

and two orders only are generated. The expressions in braces are complicated, but we know that each must be a sole associated Legendre polynomial whose order and degree match those of the spherical Bessel and trigonometric functions, respectively. It therefore remains to find their coefficients, and an easy way of doing this is to let $\theta = 90°$. Taking as an example the first brace, with the plus sign and $n+m$ even, and employing Identity [A3]:

$$\frac{(n+m)P_{n,m}(0)}{P_{n-1,m-1}(0)} = (n+m)\,\frac{1\cdot3\cdot5\cdot7\cdot\cdots(n+m-1)}{1\cdot3\cdot5\cdot7\cdot\cdots(n+m-3)} = (n+m)(n+m-1), \qquad \text{(A12)}$$

and we have the coefficient of $P_{n-1,m-1}(u)$. Similarly, taking the minus sign to obtain the coefficient of $P_{n-1,m+1}(u)$, we have:

$$\frac{(n-m)P_{n,m}(0)}{P_{n-1,m+1}(0)} = \frac{1}{2}(n-m)\,\frac{\left(\dfrac{n-m}{2}-1\right)!}{\left(\dfrac{n-m}{2}\right)!} = 1. \qquad \text{(A13)}$$

We proceed similarly for the remaining terms in Eq. [A11] and in like vein for $\sin m\phi$ spherical Bessel harmonics and the derivative in y. As the author was not able to find common identities that simplify the expressions in braces, the above results were initially obtained by expansion using Rodrigues' formula and were also found to be valid when $n+m$ was odd. However, that method, although rigorous, is extremely tedious and is not reproduced here.

By contrast, the derivative in z is easily found. The derivative with respect to r is given in Identity [A1], and Identity [A2] is also employed, as previously. We then use Identity [A4] to perform the differentiation with respect to u and Identity [A5] to convert the term involving u. Finally, attention must be paid to the values of n and m for which the formulae in Table 1 are valid; the functions η and ς perform this task.

Hertz Potential of an Elementary Loop

The Hertz potential Π of an elementary vector length $d\mathbf{s}$ of current I is given in Eq. [17] by:

$$d\Pi = -i\frac{\omega_0\mu_0 I}{4\pi k_e^2}\,\frac{e^{i(\omega_0 t - k_e R)}}{R}\,d\mathbf{s} \equiv IG(R)d\mathbf{s}. \qquad \text{(A14)}$$

With reference to Fig. 2, in spherical polar coordinates (b, α, ψ), let the unit vectors in the directions of increasing declination α and increasing azimuth ψ be $\hat{\boldsymbol{\alpha}}$ and $\hat{\boldsymbol{\psi}}$ respectively. Let a magnetic moment be created by current I flowing on the surface of the sphere round a small square of side ds. The sides are parallel to the unit vectors. Then in the limit as ds tends to zero and Ids^2 tends to a constant magnetic moment m, the Hertz potential is:

$$\Pi = -I(\nabla G\cdot ds\hat{\boldsymbol{\psi}})ds\hat{\boldsymbol{\alpha}} + I(\nabla G\cdot ds\hat{\boldsymbol{\alpha}})ds\hat{\boldsymbol{\psi}} = \frac{m}{b}\left\{\frac{-1}{\sin\alpha}\frac{\partial G}{\partial\psi}\hat{\boldsymbol{\alpha}},\ \frac{\partial G}{\partial\alpha}\hat{\boldsymbol{\psi}}\right\}. \qquad \text{(A15)}$$

Now we know from Eq. [18] that the Green's function G can be expanded in terms of spherical Bessel harmonics. Thus we need to look at the effect of Eq. [A15] on the angular portions of those harmonics and to do so we use a temporary function $G' = P_{n,m}(\nu)\cos[m(\phi - \psi)]$ where $\nu = \cos\alpha$. Applying identity [A4], we have:

$$\mathbf{\Pi}' = \frac{\mathfrak{m}}{b \sin \alpha}\{mP_{n,m}(\nu)\sin[m(\phi - \psi)]\hat{\boldsymbol{\alpha}},$$

$$- (n \cos \alpha P_{n,m}(\nu) + (n + m)P_{n-1,m}(\nu))\cos[m(\phi - \psi)]\hat{\boldsymbol{\psi}}\}. \quad \text{(A16)}$$

We may now find the Cartesian components, and we choose the x component as an example. Thus:

$$\mathbf{\Pi}'_x = \frac{\mathfrak{m}}{b \sin \alpha}\{m \cos \alpha P_{n,m}(\nu)\sin[m(\phi - \psi)]\cos \psi$$

$$+ (n \cos \alpha P_{n,m}(\nu) + (n + m)P_{n-1,m}(\nu))$$

$$\times \cos[m(\phi - \psi)]\sin \psi\} \quad \text{(A17)}$$

and once again, we see that terms in ψ in degrees $(m \pm 1)$ are created. The coefficients of the terms $\cos[m\phi - (m\text{-}1)\psi]$ and $\cos[m\phi - (m+1)\psi]$ are, in order plus, minus:

$$\frac{\mathfrak{m}}{2b \sin \alpha}\{(m \pm n)\cos \alpha P_{n,m}(\nu) + (n + m)P_{n-1,m}(\nu)\}. \quad \text{(A18)}$$

Applying Identity [A6], the coefficient of $\cos[m\phi - (m-1)\psi]$ is $\mathfrak{m}(n + m)(n - m + 1)P_{n,m+1}(\nu)/2b$, while with Identity [A7], we immediately know the coefficient of $\cos[m\phi - (m+1)\psi]$. It is $\mathfrak{m}P_{n,m+1}(\nu)/2b$. Finally, to obtain the format shown in Eq. [19], the trigonometric functions in ϕ and ψ are resolved into orthogonal variables.

REFERENCES

1. Bottonley PA, Andrew ER. RF magnetic field penetration, phase shift and power dissipation in biological tissue: implications for NMR imaging. Phys Med Biol 1978;23:630–643.
2. Hoult DI, Lauterbur PC. The sensitivity of the zeugmatographic experiment involving human samples. J Magn Reson 1979;34:425–433.
3. Mansfield P, Morris PG. NMR imaging in biomedicine. New York: Academic Press; 1982.
4. Hoult DI. RF coil technology. In: Witcofski RL, Karstaedt N, Partain CL, editors. NMR imaging. Winston Salem: The Bowman Gray School of Medicine of Wake Forest University; 1982. p 33–39.
5. Alderman DW, Grant DM. An efficient decoupler coil design which reduces heating in conductive samples in superconducting spectrometers.J Magn Reson 1979;36:447–451.
6. Bydder GM, Steiner RE, Young IR, et al. Clinical NMR imaging of the brain: 140 cases. AJR 1982;139:215–236.
7. Robitaille P-ML, Abduljalil AM, Kangarlu A, et al. Human magnetic resonance imaging at 8T. NMR Biomed 1998;11:263–265.
8. Robitaille P-ML. On SARs, RF power requirements and intrinsic MRI sensitivity at 8.0 tesla. In: Proceedings of the Workshop on New Insights Into Safety and Compatibility Issues Affecting *In Vivo* MR, International Society for Magnetic Resonance in Medicine, Washington, DC, November, 1998. p 1–2.
9. Jin J. Electromagnetic analysis and design in magnetic resonance imaging. Boca Raton: CRC Press; 1999.
10. Collins CM, Li S, Smith MB. SAR and B_1 field distributions in a heterogeneous human head model within a birdcage coil. 1998;40: 847–856.
11. Edelstein WA, Glover GH, Hardy CJ, Redington RW. The intrinsic signal-to-noise ratio in NMR imaging. Magn Reson Med 1986;3: 604–618.
12. Glover GH, Hayes CE, Pelc NJ, et al. Comparison of linear and circular polarization for magnetic resonance imaging. J Magn Reson 1985;64:255–270.
13. Hoult DI, Chen C-N, Sank VJ. Quadrature detection in the laboratory frame. Magn Reson Med 1984;1:339–353.
14. Chen C-N, Hoult DI. Biomedical magnetic resonance technology. Bristol: Adam Hilger; 1989.
15. Bomsdorf H, Helzel T, Kunz D, et al. Spectroscopy and imaging with a 4 tesla whole-body MR system. NMR Biomed 1988;1;151–158.
16. Carlson JW. Power deposition and noise correlation in NMR samples. Magn Reson Med 1989;10:399–403.
17. Keltner JR, Carlson JW, Roos MS, et al. Electromagnetic fields of surface coil *in vivo* NMR at high frequencies. Magn Reson Med 1991;22:467–480.
18. Ocali O, Atalar E. Ultimate intrinsic signal-to-noise ratio in MRI. Magn Reson Med 1998;39:462–473.
19. Deslauriers R, Hoult DI. Accurate shim-coil design and magnet-field profiling by a power-minimization matrix method. J Magn Reson 1994;108A:9–20.
20. Smythe WR. Static and dynamic electricity, 3rd ed. New York: McGraw-Hill; 1968.
21. Jackson JD. Classical electrodynamics, 2nd ed. New York: Wiley; 1975.
22. Sommerfeld A. Electrodynamics. New York: Academic Press; 1964.
23. Hertz H. Die Kräfte electrischer Schwingungen, behandelt nach der Maxwell'schen Theorie. Ann D Physik Chemie 1888;36:1–22.
24. Morse PM, Feshbach H. Methods of theoretical physics. New York: McGraw-Hill; 1953.
25. Abramowitz M, Stegun I. Handbook of mathematical functions. New York: Dover; 1965.
26. Hoult DI, Richards RE. The signal-to-noise ratio of the nuclear magnetic resonance experiment. J Magn Reson 1976;24:77–85.
27. Wen H, Chesnick AS, Balaban RS. The design and test of a new volume coil for high field imaging. Magn Reson Med 1994;32:492–498.
28. Hoult DI. The principle of reciprocity in signal strength calculations—a mathematical guide. Concepts Magn Reson (in press).
29. Erdélyi A, Magnus W, Oberhettinger F, Tricomi FG. Higher transcendental functions, vol 1. New York: McGraw-Hill; 1953.
30. Sneddon IN. Special functions of mathematical physics and chemistry. Edinburgh: Oliver and Boyd; 1961.